

Analytical solutions for timelike orbits around Damour-Solodukhin wormholes

Shao-Chen Ho , Yo-Chung Ko , Tien Hsieh , and Da-Shin Lee *

*Department of Physics, National Dong Hwa University,
Hualien, Taiwan, Republic of China*

(Dated: May 22, 2026)

Abstract

We investigate timelike geodesics around Damour-Solodukhin wormholes, which are Schwarzschild-like geometries characterized by a deformation parameter λ that determines the radius of the throat, r_{th} . The radial potential admits four roots, including the throat radius itself, allowing the throat to merge with other roots and form double, triple, and quartic degeneracies. In particular, triple-root configurations associated with the throat determine the innermost stable circular orbit (ISCO), providing a potential observational distinction from Schwarzschild black holes. Using the Mino-time parametrization, we derive particle trajectories with closed-form analytical solutions in terms of incomplete elliptic integrals for both bound and unbound motion. In particular, we focus on double or triple roots are located at the throat, the azimuthal angle and coordinate time exhibit logarithmic or power-law divergences as the particle approaches the throat. By contrast, trajectories remain regular when the throat corresponds to a simple root, allowing particles to traverse smoothly between the two asymptotically flat regions. We also derive exact homoclinic solutions associated with the throat and compute the corresponding Lyapunov exponent. In addition, inspiral and plunge trajectories through the throat are analyzed. These results provide analytic insights into particle dynamics and possible observational signatures of the wormholes.

* dslee@gms.ndhu.edu.tw

I. INTRODUCTION

In general relativity, wormholes are hypothetical spacetime tunnels that connect two distant regions of the same universe-or even two different universes. Since Einstein and Rosen introduced a bridge-like construction to tame coordinate singularities [1], and Wheeler coined the term "wormhole", its variants have served as theoretical laboratories for strong gravity phenomena. The seminal work by Morris and Thorne established that, in order for a traversable wormhole to exist without a horizon, exotic matter that violates the null energy condition must be present in its throat [2]. This finding has motivated a broad body of literature studying the stabilization of such structures. For an overview, see [3]. While exotic stabilization schemes have been proposed, there is currently no evidence that wormholes exist. Among simple and analytically tractable geometries, the static Schwarzschild-like wormhole proposed by Damour and Solodukhin (DS) in [4] has emerged as a minimal deformation of the Schwarzschild geometry in which the event horizon is replaced by a throat while preserving asymptotic flatness. From an observational perspective, horizon-scale imaging by the Event Horizon Telescope (EHT) has solidified the existence of black holes as astrophysical objects [5, 6]. However, these observations also provide opportunities to test the structure of compact objects with precision. Several proposals highlight potential discriminants between wormholes and black holes. Gravitational echoes can arise from horizonless interiors [7], quasinormal spectra can encode details of the interior geometry [8, 9], shadows and strong-field lensing may be deformed by the throat [10–15]. In particular, the influence of the throat on strong gravitational lensing in Kerr-like wormholes is examined in [16]. The distinction between a true event horizon and a horizonless variant is also studied in [17, 18].

The first direct observations of gravitational waves from the merger of binary black holes open up a new frontier in gravitational wave astronomy [19–21]. One of the key sources of low-frequency gravitational waves expected to be observed by the planned space-based Laser Interferometer Space Antenna (LISA) is from extreme mass-ratio inspirals (EMRIs) [22–26]. In astrophysics, EMRIs consist of a stellar mass object orbiting around a much heavier object, and have recently received considerable attention. Motivated by EMRIs, in this work we study the analytical solutions for particle geodesics around DS-type wormholes with particular emphasis on the role of the throat. The motion of particles can be altered by the throat [27–29]. Analytical solutions for various timelike geodesics in the exterior

of Kerr-Newman black holes have been found in [30–33]. These studies have advanced beyond geodesic motion by examining the dynamics of spinning particles in the exterior of a Reissner-Nordström black hole and a Kerr-Newman black hole respectively in [34, 35]. To our knowledge, it is for the first time to derive analytical solutions for some unique orbits in DS wormhole spacetimes, which also exist in other wormhole spacetimes. We start from the line element in [4] or [7]. Spherical symmetry and stationarity of the metric give rise to two constants of motion, the energy and the angular momentum per unit particle mass (γ_m, λ_m) . Without loss of generality, we restrict the motion to the plane $\theta = \pi/2$. Apart from the equations for the azimuthal angle ϕ and the coordinate time t , the radial equation reduces to the motion in an effective potential governed by a quartic polynomial of the coordinate r . However, a unique feature of wormholes is that particles can pass through the throat into another spacetime region if certain parameters are met. Due to the symmetry of the proper distance l measured from the throat, i.e. $l \rightarrow -l$, which will be defined later, one can map the particle trajectory from one asymptotically flat region to the other. In wormhole geometries, the throat itself can be a root of the radial potential. By varying (γ_m, λ_m) , the throat may merge with other roots of the radial potential, forming double, triple, or even quartic degeneracies. These degeneracies signal special orbits, such as unstable or stable circular motions, and the innermost stable circular orbit (ISCO) pinned at the throat. The radius of the ISCO can be accessible through observation, as discussed in [36]. The nature of the ISCO of a Kerr-like wormhole has been studied from the iron line profile signature in [18].

Next, we find the analytical solutions of the particle trajectories for bound and unbound motion. For unbound motion, we examine how the azimuthal angle and coordinate time behave when the particle crosses the throat in the case that the simple, double, or triple roots are at the throat. For bound motion, we derive an analytical solution for the homoclinic orbit towards the radius of unstable circular motion pinned to the throat. This marks the onset of chaotic motion. This is the wormhole counterpart of the Kerr and Kerr-Newman black holes [32, 37]. Then, we compute the associated Lyapunov exponent as the inverse of the instability timescale for perturbations around an unstable circular orbit. We compare this value with the Lyapunov exponent of a Schwarzschild black hole, which is bounded by AdS/CFT in [38]. Another class of representative orbits for probing strong gravitational effects is inspirals. They originate near a triple root, plunge into the throat, and bounce

back and forth between two spacetime regions. These trajectories are also expected to exist in more general wormhole spacetimes. There, they could produce gravitational waves with unique characteristics that will be discussed later [39, 40].

The layout of the paper is as follows. Section II introduces the DS wormhole metric. We then derive the equations of motion, which can be rewritten as integrals of motion in Mino time. In particular, the radial equation can be expressed in a way that defines the effective potential as a function of the coordinate r . Then, the proper radial distance, which is measured from the throat, is introduced to rewrite the effective potential in terms of the proper radial distance. Section III analyzes the throat effect on timelike trajectories for unbound and bound motions and classifies double, triple, and quartic roots of the radial potential. Moreover, we develop the throat-modified triple-root conditions and focus on the throat effect on the observational ISCO. Section IV provides closed-form orbital solutions. The implications to the observations are discussed. The summary and outlook are presented in Sec. V. Appendix A presents embedding diagrams for spatial slices of the wormhole geometry. Appendix B reviews the analytic root solutions of the cubic polynomial. Appendix C details the elliptic integrals involved in this paper [41].

II. TIMELIKE GEODESIC EQUATIONS

The metric of the static Schwarzschild-like wormhole, which is proposed by Damour and Solodukhin in [4], reads as

$$ds^2 = - \left(1 - \frac{2\tilde{M}}{r} + \lambda^2 \right) d\tilde{t}^2 + \frac{dr^2}{1 - \frac{2\tilde{M}}{r}} + r^2(d\theta^2 + \sin^2\theta d\phi^2). \quad (1)$$

It reduces to the Schwarzschild metric for $\lambda = 0$. The metric of the DS wormhole in (1) can be reexpressed with new variables t and M ,

$$t \equiv \frac{\tilde{t}}{\sqrt{1 + \lambda^2}}, \quad M \equiv \frac{\tilde{M}}{1 + \lambda^2}, \quad (2)$$

as

$$ds^2 = -f(r)dt^2 + \frac{dr^2}{g(r)} + r^2(d\theta^2 + \sin^2\theta d\phi^2), \quad (3)$$

where

$$f(r) = 1 - \frac{2M}{r}, \quad g(r) = 1 - \frac{2M(1 + \lambda^2)}{r}. \quad (4)$$

The radius of the throat is determined by $g(r_{\text{th}}) = 0$ in [7] given by

$$r_{\text{th}} = 2M(1 + \lambda^2), \quad (5)$$

and the ADM mass of the DS wormhole \tilde{M} is $\tilde{M} = M(1 + \lambda^2)$ in [11].

For this asymptotically flat, static, and spherically symmetric spacetime where the metric is independent of t and ϕ , there exist conserved quantities, namely the energy E_m and the angular momentum L_m along a geodesic,

$$E_m \equiv -\xi_t^\mu u_\mu, \quad L_m \equiv \xi_\phi^\mu u_\mu. \quad (6)$$

They can be constructed by the associated Killing vectors given by

$$\xi_t^\mu = \delta_t^\mu, \quad \xi_\phi^\mu = \delta_\phi^\mu. \quad (7)$$

Without loss of generality, we consider motion on the plane $\theta = \pi/2$. Together with timelike geodesics $u^\mu u_\mu = -1$, the equations of motion can be written as first-order differential equations with respect to the proper time σ_m ,

$$\frac{r^2}{m} \frac{dr}{d\sigma_m} = \pm_r \sqrt{\tilde{R}_m(r)}, \quad (8)$$

$$\frac{r^2}{m} \frac{d\phi}{d\sigma_m} = \lambda_m, \quad (9)$$

$$\frac{r^2}{m} \frac{dt}{d\sigma_m} = r^2 \frac{\gamma_m}{f(r)} \quad (10)$$

with two normalized conserved quantities by the particle mass m ,

$$\gamma_m \equiv \frac{E_m}{m}, \quad \lambda_m \equiv \frac{L_m}{m}. \quad (11)$$

The symbol $\pm_r = \text{sign}(u^r)$ denotes the direction of the radial velocity of the particle. Then the radial potential $\tilde{R}_m(r)$ is found to be

$$\begin{aligned} \tilde{R}_m(r) &= \frac{g(r)}{f(r)} R_m(r) \\ &= \frac{g(r)}{f(r)} [r^4 \gamma_m^2 - r^2 f(r) (r^2 + \lambda_m^2)], \end{aligned} \quad (12)$$

where $g(r)/f(r)$ is written in terms of their roots as

$$\frac{g(r)}{f(r)} = \frac{r - r_{\text{th}}}{r - 2M}. \quad (13)$$

The function $R_m(r)$, which is the radial potential of the particle in a Schwarzschild black hole, has three nonzero roots, where detailed expressions can be found in Appendix B. We can write the radial potential $\tilde{R}_m(r)$ in terms of the roots of $R_m(r)$ and an additional root at the throat as

$$\tilde{R}_m(r) = \frac{(r - r_{\text{th}})}{(r - 2M)}(\gamma_m^2 - 1)r(r - r_{m1})(r - r_{m2})(r - r_{m3}). \quad (14)$$

The roots r_{m3} , r_{m2} , and r_{m1} satisfy $r_{m1} + r_{m2} + r_{m3} = -\frac{2M}{\gamma_m^2 - 1}$, and if these roots are all real, their values are in the order of $r_{m3} \geq r_{m2} \geq r_{m1}$. Here, the root at the throat radius r_{th} is treated as a free parameter, characterizing different wormholes. Eqs. (8)-(10) can be fully decoupled in terms of the Mino time τ_m defined as [42]

$$\frac{dx^\mu}{d\tau_m} \equiv \frac{r^2}{m} \frac{dx^\mu}{d\sigma_m}. \quad (15)$$

For the source point x_i^μ and the observer point x^μ , the integral forms of the equations can be expressed as

$$\tau_m - \tau_{mi} = I_r, \quad (16)$$

$$\phi - \phi_i = \lambda_m I_r, \quad (17)$$

$$t - t_i = \gamma_m I_t, \quad (18)$$

where the integrals I_r and I_t involve the radial potential $\tilde{R}_m(r)$, given by

$$I_r(r) = \int_{r_i}^r \frac{1}{\sqrt{\tilde{R}_m(r)}} dr, \quad (19)$$

$$I_t(r) = \int_{r_i}^r \frac{r^2}{f(r)\sqrt{\tilde{R}_m(r)}} dr. \quad (20)$$

The radial equation in (8) can also be expressed in the form

$$\left(\frac{dr}{d\sigma_m}\right)^2 + V_{\text{eff}}(r) = 0 \quad (21)$$

from which to define the effective potential $V_{\text{eff}}(r)$ as

$$V_{\text{eff}}(r) = -g(r) \left(\frac{\gamma_m^2}{f(r)} - \frac{\lambda_m^2}{r^2} - 1 \right). \quad (22)$$

Now we introduce a proper radial distance l from the throat given by

$$\begin{aligned} l &\equiv \pm \int_{r_{\text{th}}}^r \sqrt{\frac{1}{g(r)}} dr \\ &= \sqrt{r^2 - 2M(1 + \lambda^2)r} + M(1 + \lambda^2) \log \left(\frac{r - M(1 + \lambda^2) + \sqrt{r^2 - 2M(1 + \lambda^2)r}}{M(1 + \lambda^2)} \right), \end{aligned} \quad (23)$$

where the value of l is defined in the range of $-\infty < l < \infty$ and the throat is located at $l = 0$. Furthermore, Eq. (21) can be rewritten in terms of the proper radial distance to be

$$\dot{l}^2 + \tilde{V}_{\text{eff}}(l) = 0, \quad (24)$$

where

$$\tilde{V}_{\text{eff}}(l) = -g(l) \left(\frac{\gamma_m^2}{f(l)} - \frac{\lambda_m^2}{r(l)^2} - 1 \right). \quad (25)$$

The effective potentials above will be used to examine the different types of trajectories to obtain their analytical solutions.

III. ANALYSIS OF THE ROOTS OF THE RADIAL POTENTIAL

A noteworthy feature of wormhole spacetimes is that the throat is one of the roots of the radial potential. The root at the throat can merge with the other roots to form double, triple, or even quartic roots. These degeneracies result in unique particle trajectories in wormholes compared to black holes. To analyze this phenomenon, we classify particle trajectories as bound ($\gamma_m^2 < 1$) or unbound ($\gamma_m^2 > 1$) motion. First, we find the parameters γ_m , λ_m , and r_{th} , which lead to the double roots, namely $r_{\text{th}} = r_{m3}$ or $r_{\text{th}} = r_{m2}$, where r_{m3} and r_{m2} are the two outermost roots of the radial potential $R_m(r)$. We will also find the parameters for the triple roots $r_{\text{th}} = r_{m3} = r_{m2}$ and the quartic root $r_{\text{th}} = r_{m3} = r_{m2} = r_{m1}$. The latter arises only for bound orbits.

A. Unbound motion for $\gamma_m^2 > 1$

We first consider the double-root condition of $\tilde{R}_m(r)$, that is,

$$\tilde{R}_m(r) = 0 \quad \text{and} \quad \tilde{R}'_m(r) = 0 \quad (26)$$

under which the wormhole throat coincides with the root of r_{m3} or r_{m2} , satisfying

$$r_m = r_{\text{th}}, \quad R_m(r_m) = 0. \quad (27)$$

Solving the double-root condition (27) with given R_m in (12), we can obtain the relation

$$\lambda_{m(\text{th})} = r_{m(\text{th})} \sqrt{\frac{r_{m(\text{th})}(\gamma_m^2 - 1) + 2M}{r_{m(\text{th})} - 2M}}, \quad (28)$$

where the subscript $m(\text{th})$ denotes double-root solutions involving the throat. Then, Eq. (28) is used to construct the parameter space diagram $\lambda_{m(\text{th})}-r_{\text{th}}$ in Fig. 1 in a solid (dash) blue line for unstable (stable) double roots at $r_{m2} < r_{\text{th}} = r_{m3}$ ($r_{\text{th}} = r_{m2} < r_{m3}$). Additionally, the solid (dash) red line represents the parameters for the stable (unstable) double roots at $r_{m3} = r_{m2}$, where the throat radius satisfies $r_{\text{th}} > r_{m3} = r_{m2}$ ($r_{\text{th}} < r_{m3} = r_{m2}$). Two lines for $r_{m2} < r_{\text{th}} = r_{m3}$, $r_{\text{th}} > r_{m3} = r_{m2}$ ($r_{\text{th}} = r_{m2} < r_{m3}$, $r_{\text{th}} < r_{m3} = r_{m2}$) merge at the triple roots, namely $r_t \equiv r_{\text{th}} = r_{m3} = r_{m2}$ determined by the triple-root condition $\tilde{R}_m(r_{\text{th}}) = \tilde{R}'_m(r_{\text{th}}) = \tilde{R}''_m(r_{\text{th}}) = 0$ or $r_t = r_{\text{th}}$, $R_m(r_{\text{th}}) = 0$, $R'_m(r_{\text{th}}) = 0$ with the parameters

$$\lambda_t = \frac{\sqrt{M} r_t}{\sqrt{r_t - 3M}}, \quad \gamma_t = \frac{r_t - 2M}{\sqrt{(r_t - 3M) r_t}}, \quad (29)$$

which are marked by a black point in Fig. 1. Notice that this also refers to the solutions of the double root $r_{m3} = r_{m2} \neq r_{\text{th}}$ or $r_{m1} = r_{m2} \neq r_{\text{th}}$ denoted in general by r_{mc} with the parameters

$$\lambda_{\text{mc}} = \frac{\sqrt{M} r_{\text{mc}}}{\sqrt{r_{\text{mc}} - 3M}}, \quad \gamma_{\text{mc}} = \frac{r_{\text{mc}} - 2M}{\sqrt{(r_{\text{mc}} - 3M) r_{\text{mc}}}}. \quad (30)$$

The effective potentials $V_{\text{eff}}(r)$ and $\tilde{V}_{\text{eff}}(l)$ of the parameters at the highlighted points in this diagram are shown in Fig. 2. We emphasize some of the parameter points, with which to give rise to a unique trajectory in the wormhole spacetime. The parameters at the orange (black) point are for the double roots at $r_{\text{th}} = r_{m3} > r_{m2}$ in Sec. IV A (the triple roots at $r_{\text{th}} = r_{m3} = r_{m2}$ in Sec. IV B), where the particle starts from spatial infinity and takes an infinite amount of time to reach the throat. The parameters at the blue point depict $r_{\text{th}} > r_{m3} = r_{m2}$ in Sec. IV C, where the particle travels from spatial infinity and then smoothly passes through the throat.

Having delineated the unbound motion, we next consider the bound motion analysis ($\gamma_m^2 < 1$), where quartic roots can arise. In the next section, we present the analysis of the parameters to construct the corresponding parameter diagram in Fig. 3.

B. Bound motion for $\gamma_m^2 < 1$

We now construct a diagram of the parameter space for the bound motion with $\gamma_m^2 < 1$. To proceed, let us remind that for the double roots, $r_{m3} = r_{m2}$ and $r_{m2} = r_{m1}$, shown in

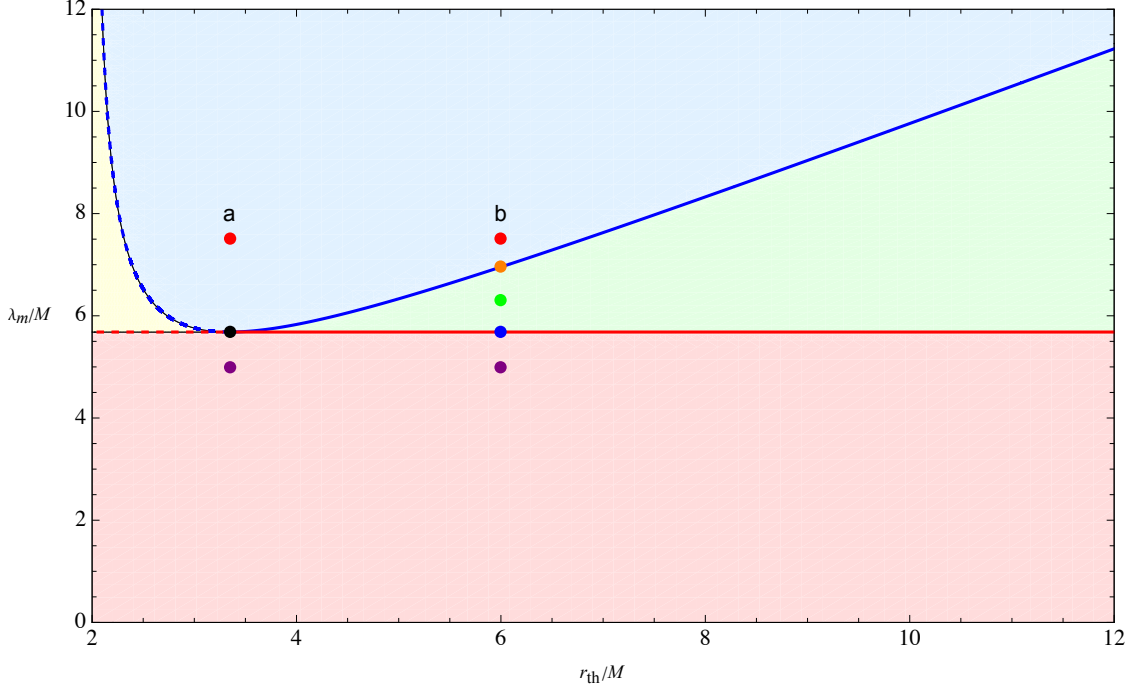


FIG. 1. A diagram of the parameter space $(\lambda_m, r_{\text{th}})$ for a particle's unbound motion in wormhole geometry with fixed energy $\gamma_m = 1.25$. The blue dashed (solid) curve represents the parameters for the double roots $r_{m2} = r_{\text{th}}$ ($r_{m3} = r_{\text{th}}$), while the red dashed (solid) curve corresponds to the parameters for the double roots $r_{m2} = r_{m3} > r_{\text{th}}$ ($r_{m2} = r_{m3} < r_{\text{th}}$). All four curves merge at the triple root, $r_{m2} = r_{m3} = r_{\text{th}}$, indicating a special end point of these radii. The color-shaded regions illustrate distinct types of $(r_{\text{th}}, r_{m2}, r_{m3})$: light yellow for $r_{\text{th}} < r_{m2} < r_{m3}$; blue for $r_{m2} < r_{\text{th}} < r_{m3}$; light green for $r_{m2} < r_{m3} < r_{\text{th}}$; light red for the complex-conjugate pair $r_{m2} = r_{m3}^*$. Notice that the root r_{m1} always lies within the throat radius. Highlighted points in this diagram exemplify special orbits discussed in the text. The black point denotes the parameters with the unique triple-root solution in Sec. IV B. The orange point marks the parameters for an unstable circular orbit with $r_{\text{th}} = r_{m3} > r_{m2}$ in Sec. IV A, and the blue point depicts the parameters for $r_{\text{th}} > r_{m3} = r_{m2}$ in Sec. IV C. These particular parameters are used to investigate special particle trajectories affected by the throat. Additionally, the separate points shown in columns (a) and (b) reflect two different radii of the wormhole throat, by varying the particle's angular momentum. Their respective effective potentials, in terms of both the radial coordinate r and the proper distance l , appear in Fig. 2.

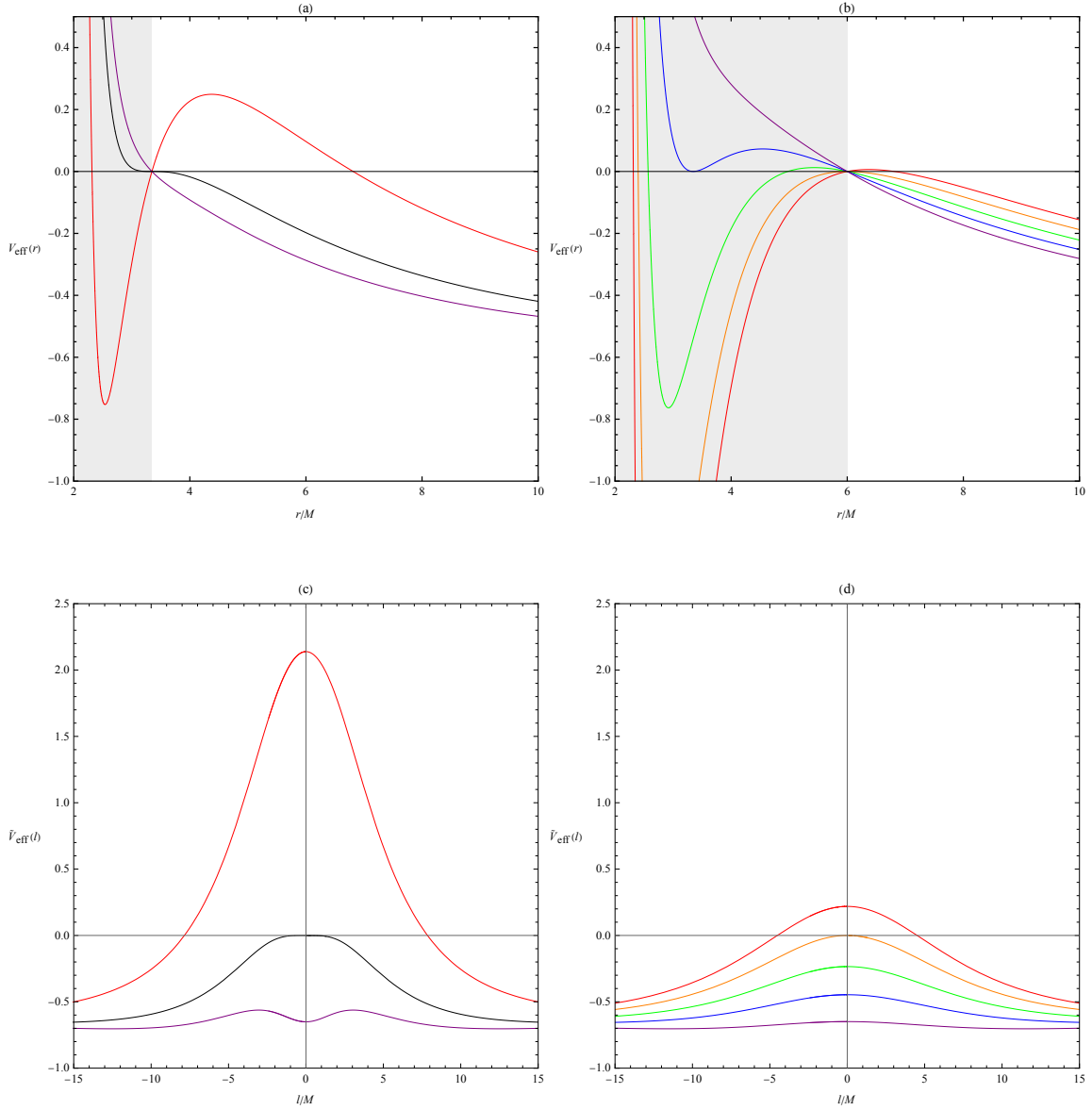


FIG. 2. Effective potentials $V_{\text{eff}}(r)$ as a function of the dimensionless radius r/M , and $\tilde{V}_{\text{eff}}(l)$ as a function of the dimensionless proper distance l/M , computed using the parameters as in Fig. 1. In panels (a) and (c), the red, black, and purple curves of the effective potentials are due to the parameters at the same colored points in column (a) of Fig. 1. Likewise, panels (b) and (d) showcase the effective potential for the parameter set in column (b) of Fig. 1. The effective potentials in the orange, black, and blue lines will be discussed in Secs. IV A, IV B, and IV C, respectively.

Appendix B with the parameters along the solid blue and red curves respectively in Fig. 3, the root conditions give the relation between γ_m and λ_m in (30). For the triple roots at $r_{m1} = r_{m2} = r_{m3}$, which is known as $r_{\text{isco}} = 6M$, when the double roots at $r_{m3} = r_{m2}$ and $r_{m2} = r_{m1}$ merge, the values of γ_m and λ_m are $\gamma_m = 2\sqrt{2}/3$ and $\lambda_m = 2\sqrt{3}M$, respectively. To study interesting particle orbits, we will restrict ourselves to the case of $\gamma_m \geq 2\sqrt{2}/3$. Following the double roots and triple roots conditions involving the throat in (28) and (29), the parameters lead to various types of the roots. In each panel of Fig. 3, the red dashed curves correspond to the parameters with the stable double root at the throat with $r_{m1} = r_{\text{th}}$, while the blue dashed curves denote the parameters with the other stable double root with $r_{m3} = r_{\text{th}}$.

For $\gamma_m > 2\sqrt{2}/3$, there is the unstable double root at $r_{m2} = r_{\text{th}}$ with the parameters marked in purple curves. The parameters with the two distinct triple roots, $r_{\text{th}} = r_{m3} = r_{m2}$ at the blue point and $r_{\text{th}} = r_{m2} = r_{m1}$ at the red point, appear in the left panel. For a given energy parameter $\gamma_m > 2\sqrt{2}/3$, there is a range of the r_{th} values, which admit the double root. Specifically, the end points of the purple curve in Fig. 3(a) are determined by plugging (28) in (29) giving

$$\frac{M \left[4 - \gamma_m \left(3\gamma_m + \sqrt{9\gamma_m^2 - 8} \right) \right]}{2(1 - \gamma_m^2)} < r_{\text{th}} = r_{m2} < \frac{M \left[4 - \gamma_m \left(3\gamma_m - \sqrt{9\gamma_m^2 - 8} \right) \right]}{2(1 - \gamma_m^2)}. \quad (31)$$

Moreover, the end points of the double root $r_{m3} = r_{\text{th}}$ are given by

$$\frac{M \left[4 - \gamma_m \left(3\gamma_m - \sqrt{9\gamma_m^2 - 8} \right) \right]}{2(1 - \gamma_m^2)} \leq r_{m(\text{th})} = r_{m3} \leq \frac{2M}{1 - \gamma_m^2}, \quad (32)$$

whose upper bound is determined when $\lambda_m \rightarrow 0$ in (28). The effective potentials, plotted as functions of coordinate r and proper distance l , are shown in Fig. 4.

Figure 3(b) shows a diagram of the parameter space when $\gamma_m = 2\sqrt{2}/3$. In this case, the double roots at $r_{m3} = r_{m2}$ and $r_{m2} = r_{m1}$ merge, further resulting in the merging of the triple roots $r_{\text{th}} = r_{m3} = r_{m2}$ and $r_{\text{th}} = r_{m2} = r_{m1}$ to form a unique quartic root, which parameters are labeled by a black point. The nature of all the roots in the shaded areas is described in the figure caption. Here we focus on the parameter space where the roots are all real.

One of the most interesting trajectories for the bound motion is the homoclinic orbit. A homoclinic orbit towards the throat at the double root $r_{\text{th}} = r_{m2}$ is with the parameters

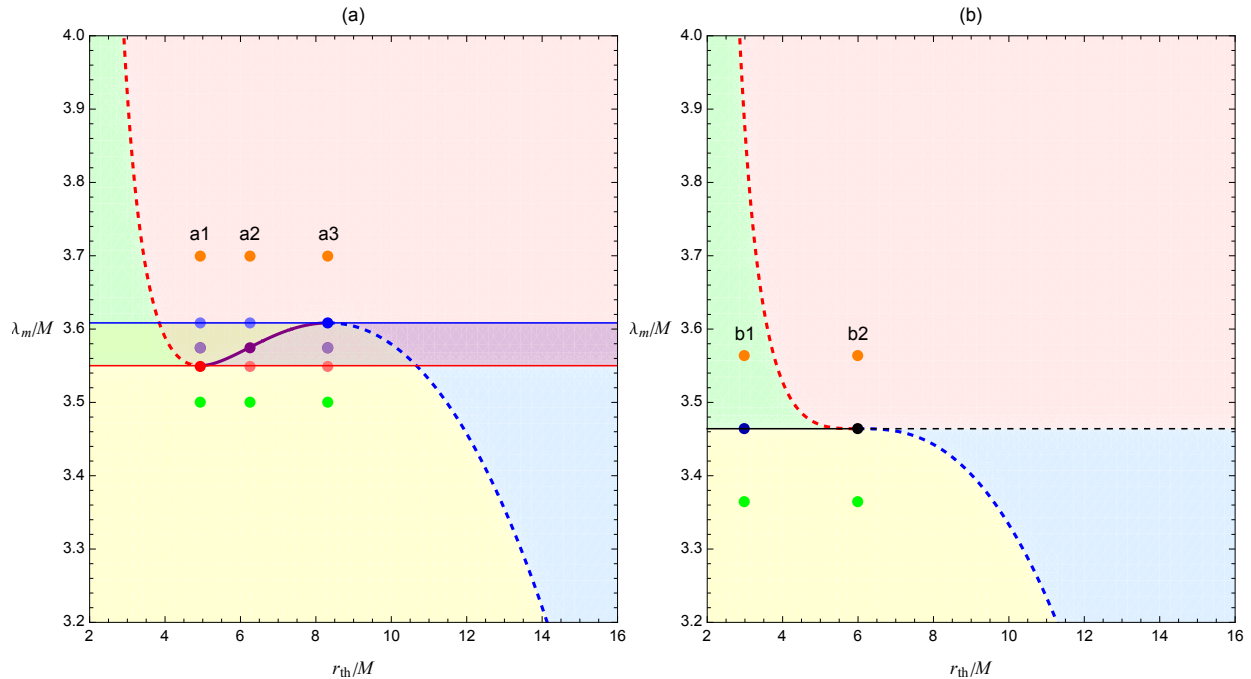


FIG. 3. A diagram of the parameter space $(\lambda_m, r_{\text{th}})$ for a particle's bound motion in wormhole geometry with fixed value of γ_m where $\gamma_m = 0.95 > 2\sqrt{2}/3$ in panel (a) and $\gamma_m = 2\sqrt{2}/3$ in panel (b). In each panel, the parameters in red (blue) dashed curves correspond to the stable double roots at the throat with $r_{m1} = r_{\text{th}}$ ($r_{m3} = r_{\text{th}}$), while those in solid purple curves are for the unstable double root at $r_{m2} = r_{\text{th}}$ in Sec. IV D. In addition, the parameters in solid red (blue) curves are due to the double roots at $r_{m1} = r_{m2}$ ($r_{m3} = r_{m2}$). The parameters in the light green region satisfy $r_{\text{th}} < r_{m1}$ with $r_{m2} = r_{m3}^*$, in the light red region $r_{\text{th}} > r_{m1}$ with $r_{m2} = r_{m3}^*$, in the light yellow region $r_{\text{th}} < r_{m3}$ with $r_{m1} = r_{m2}^*$, and in the blue region $r_{\text{th}} > r_{m3}$ with $r_{m1} = r_{m2}^*$. Panel (a): For $\gamma_m > 2\sqrt{2}/3$, the parameters with two distinct triple-root solutions appear at blue and red points. The blue point in column (a3) ($r_{\text{th}} = r_{m3} = r_{m2}$) and the red point in column (a1) ($r_{\text{th}} = r_{m2} = r_{m1}$) partition the diagram into four additional color-shaded regions from left to right with the different orderings: $r_{\text{th}} < r_{m1} < r_{m2} < r_{m3}$, $r_{m1} < r_{\text{th}} < r_{m2} < r_{m3}$, $r_{m1} < r_{m2} < r_{\text{th}} < r_{m3}$, and $r_{m1} < r_{m2} < r_{m3} < r_{\text{th}}$. Panel (b): At the critical value $\gamma_m = 2\sqrt{2}/3$, the red and blue dashed and solid curves merge at a single quartic-root point (black point) of $r_{\text{th}} = r_{m3} = r_{m2} = r_{m1}$ along the gray line. The parameters in solid (dashed) line correspond to $r_{\text{th}} < r_{m3} = r_{m2} = r_{m1}$ ($r_{\text{th}} > r_{m3} = r_{m2} = r_{m1}$) in Sec. IV E.

shown in the purple solid curve in Fig. 3(a). Its analytic solution and orbital diagram will be presented later in Sec. IV D. Another noteworthy trajectory is the inspiral orbit

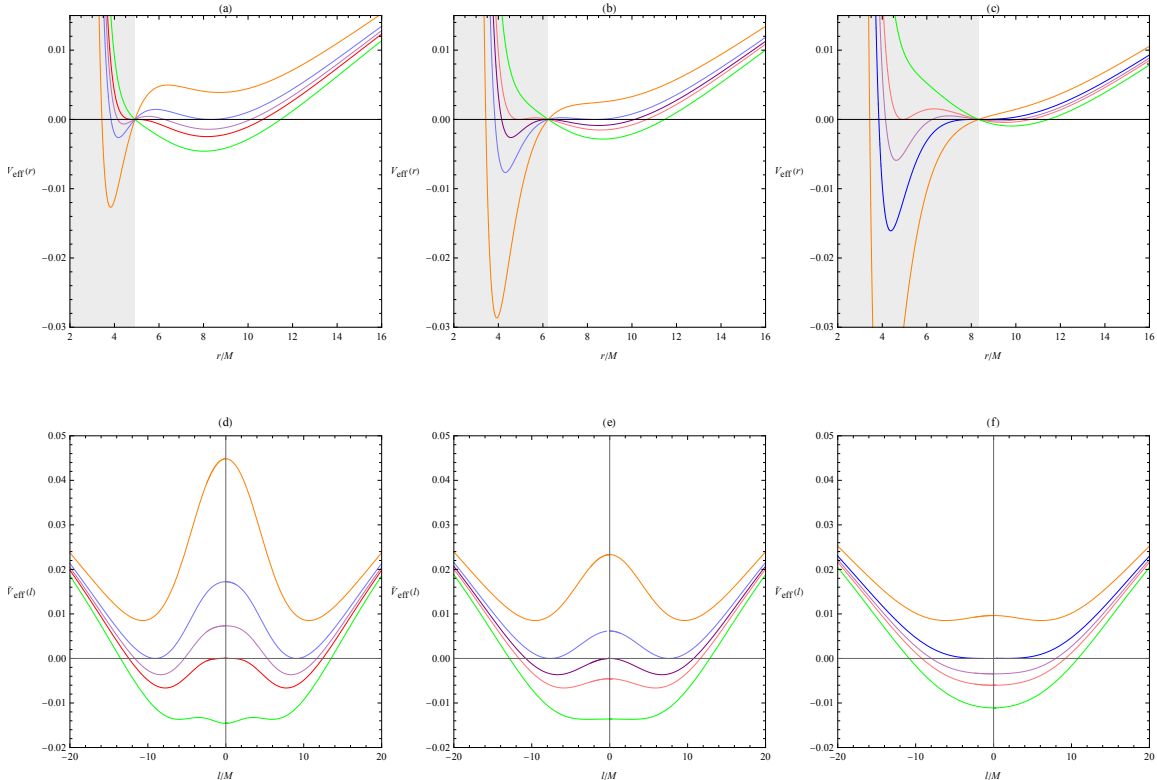


FIG. 4. Effective potentials $V_{\text{eff}}(r)$ as a function of the dimensionless radius r/M , and $\tilde{V}_{\text{eff}}(l)$ as a function of the dimensionless proper distance l/M , computed for the same energy per unit mass $\gamma_m = 0.95$ and the parameters shown in Fig. 3(a). The effective potential in purple line, which corresponds to the homoclinic orbit in (b) and (e), will be discussed in Sec. IV D.

with the parameters highlighted by the deep blue point in Fig. 3(b) with the effective potentials in Fig. 5(a) and (c). For this orbit, the particle initially resides near the triple root $r_i \lesssim r_{m3} = r_{m2} = r_{m1}$ and then spirals towards the throat. A complete analytical treatment of these solutions will be presented in the following section.

Next, we will conduct a thorough analysis of triple and quartic root configurations, focusing on their potential observational signatures that could distinguish between wormholes and black holes.

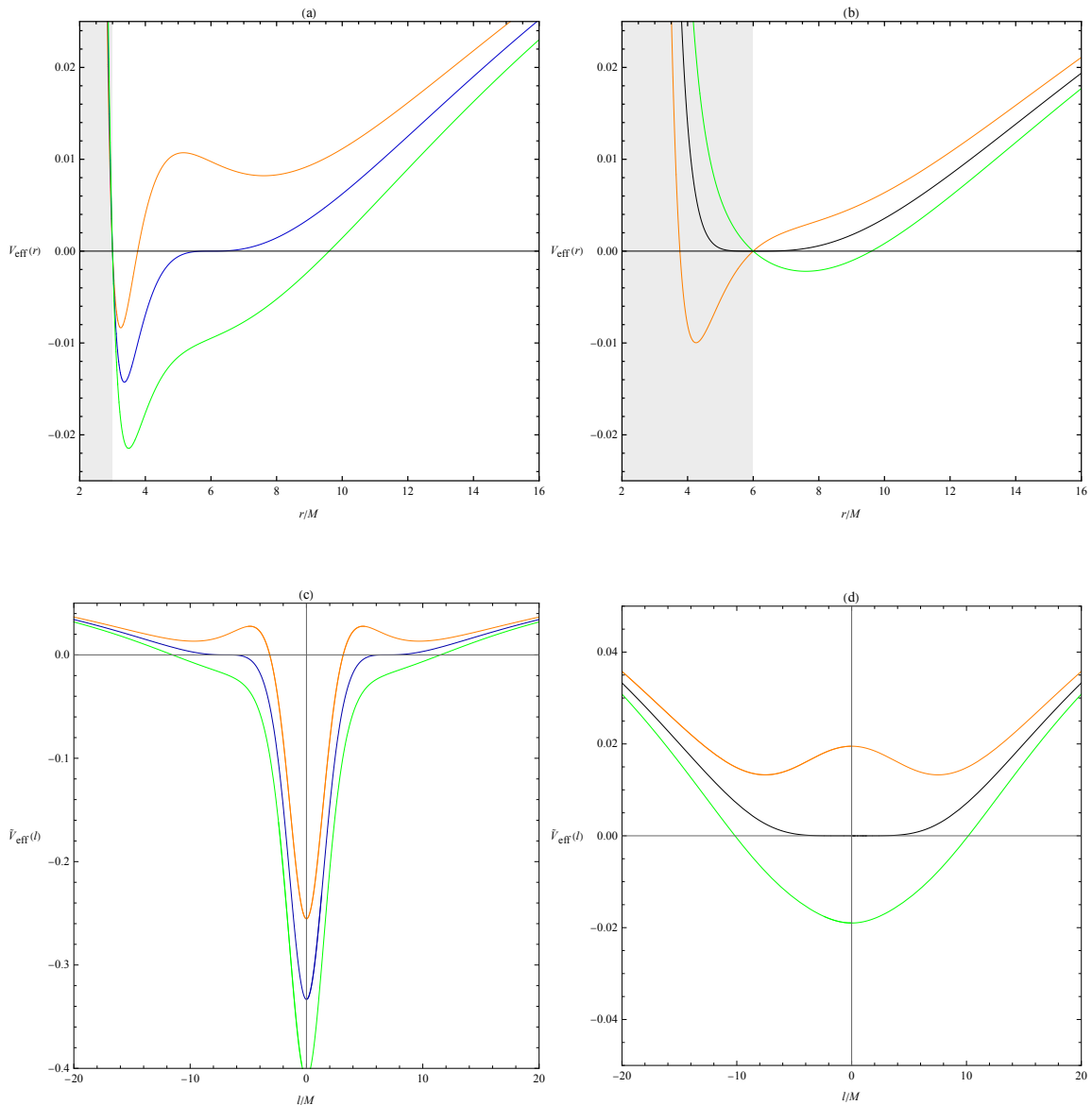


FIG. 5. Effective potentials $V_{\text{eff}}(r)$ as a function of the dimensionless radius r/M , and $\tilde{V}_{\text{eff}}(l)$ as a function of the dimensionless proper distance l/M , computed at the energy $\gamma_m = 2\sqrt{2}/3$ and with the parameters used in Fig. 3(b). The effective potential in the blue line, which corresponds to the inspiral orbit, will be discussed in Sec. IV E.

C. Triple and Quartic Roots

We consider a special orbit that could be observationally accessible, namely the innermost stable circular orbit (ISCO) using the throat radius r_{th} as a free parameter. Here we

investigate how an ISCO radius might be modified by a wormhole, which can be used to distinguish between wormholes with the metric for $\lambda \neq 0$ from black holes with the metric for $\lambda = 0$. Let us consider a diagram of the parameter space for the double root r_{mc} given by r_{m1}, r_{m2}, r_{m3} versus λ_{mc} with varied γ_{mc} , following (30). In Fig. 6, the parameters in the solid blue line are for the stable double root $r_{\text{mcs}} \equiv r_{m3} = r_{m2} > 6M$. The radius of a stable circular motion is determined by these outermost double root $r_{\text{mcs}} = r_{m3} = r_{m2}$ with a given either γ_m or λ_m in (30). Starting from a given throat radius with $6M < r_{\text{th}} < r_{\text{mcs}}$, the radius r_{mcs} can decrease as either λ_m or γ_m decreases along the solid blue line in Fig. 6 until r_{mcs} meets the throat r_{th} to form the triple roots with the solution in (29). The radius of this triple root is the radius of the ISCO. However, the radius at $r_{\text{isco}} \equiv r_{m3} = r_{m2} = r_{m1} = 6M$ with $\lambda_m = 2\sqrt{3}M$ and $\gamma_m = 2\sqrt{2}/3$ labeled by the point Q is a triple root of the radial potential $\tilde{R}_m(r)$ when $r_{\text{th}} \neq 6M$, which is also the radius of the ISCO for the $\lambda = 0$ metric in (3) of a Schwarzschild black hole. Thus, one can distinguish wormhole spacetimes from those of black holes by observing the radius of the ISCO at the throat with particular choice of λ_m and γ_m in the blue line as long as $r_{\text{th}} > 6M$. The triple roots at the throat may provide a potentially observable signature for identifying wormhole geometries in an astrophysical observation. If r_{th} is located at point Q, this gives a quartic root. In addition, the parameters in the solid red curve are for the unstable double root at $r_{m2} = r_{m1}$. Although the throat at $r_{\text{th}} < 6M$ can be the triple root at $r_{\text{th}} = r_{m2} = r_{m1}$, the radius of the ISCO in the wormholes is determined by the triple roots at $r_{m3} = r_{m2} = r_{m1} = 6M$, making it indistinguishable from that of a black hole. For completeness, when the solid red line crosses the horizontal dashed gray line at $r = 4M$ in the case of $\gamma_m = 1$ by increasing either γ_m or λ_m , the motion changes from bounded to unbounded motion. In the unbound motion, as γ_m increases to infinity, the dashed blue curve for the double root $r_{m3} = r_{m2}$ approaches the line of $r = 3M$, which corresponds to the radius of the photon sphere for the null geodesics.

IV. ANALYTICAL ORBITAL SOLUTIONS

In this section, we derive analytical solutions for the trajectories of the particles, including the bound and unbound motion. Due to the spherical symmetry of the Schwarzschild-like wormhole spacetime, we consider the orbits in the plane of $\theta = \pi/2$ with the solutions for the azimuthal angle ϕ and coordinate time t expressed as a function of the radial coordinate

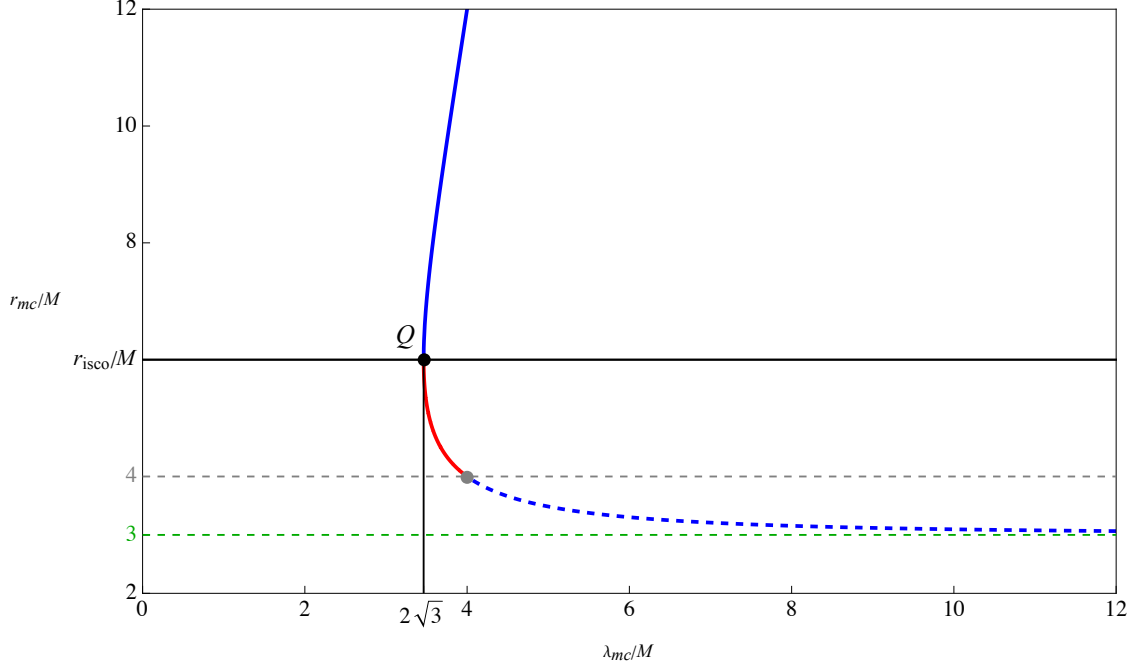


FIG. 6. This is a parameter-space diagram showing all possible double-root solutions for r_{mc} given by r_{m1}, r_{m2}, r_{m3} of a function of λ_{mc} with the varied γ_{mc} values, using (30). The solid blue curve is for the bound motion ($\gamma_m < 1$) with the parameters at $r_{mcs} \equiv r_{m3} = r_{m2}$. The solid red curve is also for the bound motion ($\gamma_m < 1$) but with the parameters at $r_{mcs} \equiv r_{m1} = r_{m2}$. Two double root lines merges at the point Q which means the triple root $r_{m1} = r_{m2} = r_{m3} = 6M$ with $\gamma_m = 2\sqrt{2}/3$. The value of γ_m can increase from $\gamma_m < 1$ to $\gamma_m > 1$ that crosses the horizontal dashed grey line at $r = 4M$ for $\gamma_m = 1$. For this unbound motion, as γ_m increases to infinity, the dashed blue curve representing the unstable double root $r_{m3} = r_{m2}$ will asymptote to the green line of $r = 3M$, which corresponds to the radius of the photon sphere for the null geodesics.

r . Following the integral (19) and (20), the solutions of $\phi(r)$ and $t(r)$ can be expressed as elliptic integrals. We present the unique trajectories related to the throat of the wormhole with the parameters in Fig. 1.

A. $r_{th} = r_{m3}$

We consider the double root with the parameters at the orange point in Fig. 1. For the unbound motion ($\gamma_m^2 > 1$) the particle starts from spatial infinity and approaches the throat at the double root based on the effective potential shown in Fig. 4. The solutions of $\phi^A(r)$

and $t^A(r)$ are given by the elliptic integrals as

$$\phi^A(r) = \nu_{r_i} \frac{2\lambda_m}{\sqrt{(\gamma_m^2 - 1)(2M - r_{m1})r_{m2}}} \left[\frac{2M - r_{m2}}{r_{\text{th}} - r_{m2}} \Pi(\alpha^A; \psi^A(r)|k^A) \right] - \phi_i^A, \quad (33)$$

$$\begin{aligned} t^A(r) = & \nu_{r_i} \frac{\gamma_m}{\sqrt{\gamma_m^2 - 1}} \left\{ \sqrt{\frac{r(r - r_{m2})(r - r_{m1})}{r - 2M}} + \frac{1}{\sqrt{(2M - r_{m1})r_{m2}}} \left[(r_{m1} - 2M)r_{m2} E(\psi^A(r)|k^A) \right. \right. \\ & + \frac{8M^3 + r_{\text{th}}r_{m1}r_{m2} + 4M^2(r_{m1} + r_{m2} + r_{\text{th}}) - 2M[r_{m1}r_{m2} + r_{\text{th}}(r_{m1} + r_{m2})]}{2M - r_{\text{th}}} F(\psi^A(r)|k^A) \\ & \left. \left. + (r_{m2} - 2M)(2M + r_{m1} + r_{m2} + 2r_{\text{th}}) \Pi(\beta^A; \psi^A(r)|k^A) + \frac{2r_{\text{th}}^3(2M - r_{m2})}{(2M - r_{\text{th}})(r_{m2} - r_{\text{th}})} \Pi(\alpha^A; \psi^A(r)|k^A) \right] \right\} - t_i^A, \quad (34) \end{aligned}$$

where

$$\begin{aligned} \psi^A(r) &= \sin^{-1} \sqrt{\frac{(r - r_{m2})(2M - r_{m1})}{(r - 2M)(r_{m2} - r_{m1})}}; & k^A &= \frac{2M(r_{m2} - r_{m1})}{r_{m2}(2M - r_{m1})}; & \nu_{r_i} &= -1; \\ \alpha^A &= \frac{(r_{\text{th}} - 2M)(r_{m2} - r_{m1})}{(r_{\text{th}} - r_{m2})(2M - r_{m1})}; & \beta^A &= \frac{r_{m2} - r_{m1}}{2M - r_{m1}}, \end{aligned} \quad (35)$$

and $F(\varphi|k)$, $E(\varphi|k)$, and $\Pi(\alpha; \varphi|k)$ are the incomplete elliptic integrals of the first, second, and third kinds, respectively, introduced in Appendix C. The trajectory in an embedded diagram is shown in Fig. 7.

One advantage of the analytical formulas is to explore $\phi(r)$ and $t(r)$ as the particle approaches the throat. As $r \rightarrow r_{\text{th}}$, the elliptic integral Π in (33) and (34) shows a logarithmic divergence, giving $\phi^A \sim \log(r - r_{\text{th}})$ and $t^A \sim \log(r - r_{\text{th}})$ due to the fact that the throat is at the double root.

B. $r_{\text{th}} = r_{m3} = r_{m2}$

In this case, we consider a triple root located at the throat, where no analogous triple-root configuration exists for the unbound motion in black holes with the $\lambda = 0$ metric in (3). The particle also starts from spatial infinity and moves toward the triple roots at the throat. Using the solution in Sec. IV A, its analytical solutions can be achieved in the limit of $r_{m2} \rightarrow r_{\text{th}}$. In this limit, according to Appendix C, the terms involving $\Pi(\alpha^A; \psi^A(r)|k^A)$ in (33) and (34) reduce to

$$\frac{2M - r_{m2}}{r_{\text{th}} - r_{m2}} \Pi(\alpha^A; \psi^A(r)|k^A) \rightarrow \frac{2M - r_{m1}}{r_{\text{th}} - r_{m1}} H(\psi^B(r)|k^B), \quad (36)$$

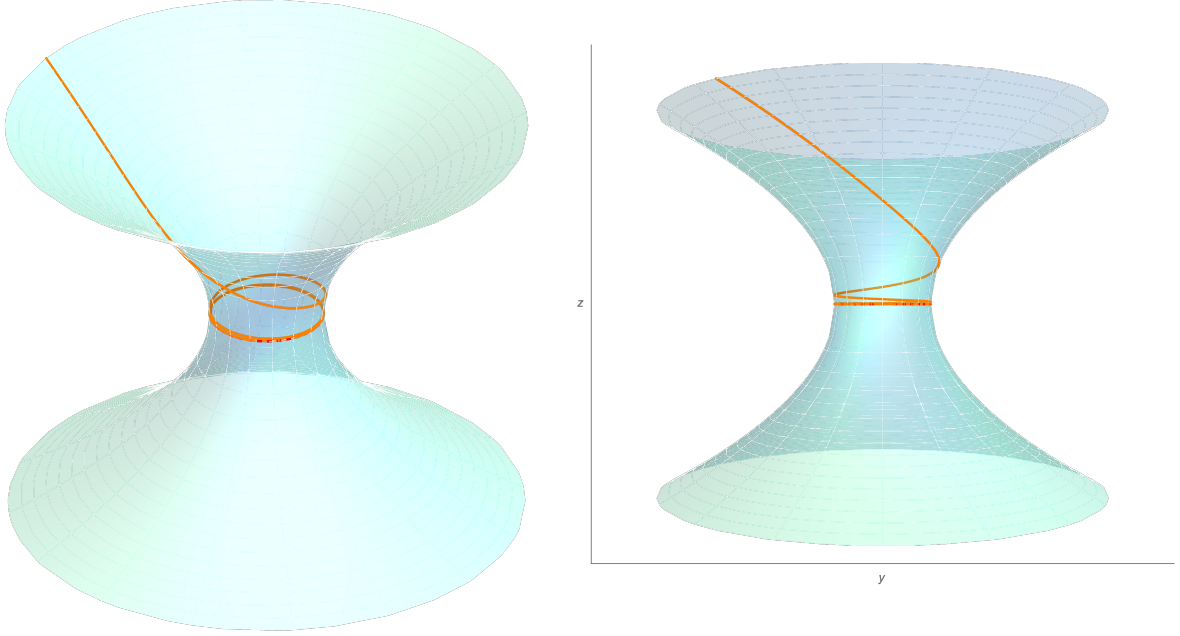


FIG. 7. Embedding diagram onto which the particle trajectory is projected. The particle with the parameters at the orange point in column (b) of Fig. 1 giving $r_{\text{th}} = r_{m3}$, begins at spatial infinity and evolves toward the throat-involved unstable double root (the red dashed circle). Note that, the trajectory is located on the plane $\theta = \pi/2$, and is projected onto a 2-D surface in Appendix A.

and

$$\frac{2r_{\text{th}}^3(2M - r_{m2})}{(r_{\text{th}} - 2M)(r_{\text{th}} - r_{m2})} \Pi(\alpha^A; \psi^A(r)|k^A) \rightarrow \frac{2r_{\text{th}}^3(2M - r_{m1})}{(r_{\text{th}} - 2M)(r_{\text{th}} - r_{m1})} H(\psi^B(r)|k^B), \quad (37)$$

where $H(\psi^B|k^B)$ is defined in (C3). The analytic solutions are summarized as

$$\phi^B(r) = \nu_{r_i} \frac{2\lambda_m}{\sqrt{(\gamma_m^2 - 1)(2M - r_{m1})r_{\text{th}}}} \left[\frac{2M - r_{m1}}{r_{\text{th}} - r_{m1}} H(\psi^B(r)|k^B) \right] - \phi_i^B, \quad (38)$$

$$t^B(r) =$$

$$\begin{aligned} & \nu_{r_i} \frac{\gamma_m}{\sqrt{\gamma_m^2 - 1}} \left\{ \sqrt{\frac{r(r - r_{\text{th}})(r - r_{m1})}{r - 2M}} + \frac{1}{\sqrt{(2M - r_{m1})r_{\text{th}}}} \left[(r_{m1} - 2M)r_{\text{th}} E(\psi^B(r)|k^B) \right. \right. \\ & + \frac{8M^3 + r_{m1}r_{\text{th}}^2 + 4M^2(r_{m1} + 2r_{\text{th}}) - 2M[r_{m1}r_{\text{th}} + r_{\text{th}}(r_{m1} + r_{\text{th}})]}{2M - r_{\text{th}}} F(\psi^B(r)|k^B) \\ & \left. \left. + (r_{\text{th}} - 2M)(2M + r_{m1} + 3r_{\text{th}}) \Pi(\beta^B; \psi^B(r)|k^B) + \frac{2r_{\text{th}}^3(2M - r_{m1})}{(r_{\text{th}} - 2M)(r_{\text{th}} - r_{m1})} H(\psi^B(r)|k^B) \right] \right\} - t_i^B, \quad (39) \end{aligned}$$

where

$$H(\psi^B(r)|k^B) = \Pi(1; \psi^B(r)|k^B) - \cot \psi^B(r) \sqrt{1 - k^B \sin^2 \psi^B(r)} \quad (40)$$

and

$$\psi^B(r) = \sin^{-1} \sqrt{\frac{(r - r_{\text{th}})(2M - r_{m1})}{(r - 2M)(r_{\text{th}} - r_{m1})}}; \quad k^B = \frac{2M(r_{\text{th}} - r_{m1})}{r_{\text{th}}(2M - r_{m1})}; \quad \beta^B = \frac{r_{\text{th}} - r_{m1}}{2M - r_{m1}}. \quad (41)$$

The trajectory is illustrated in Fig. 8.

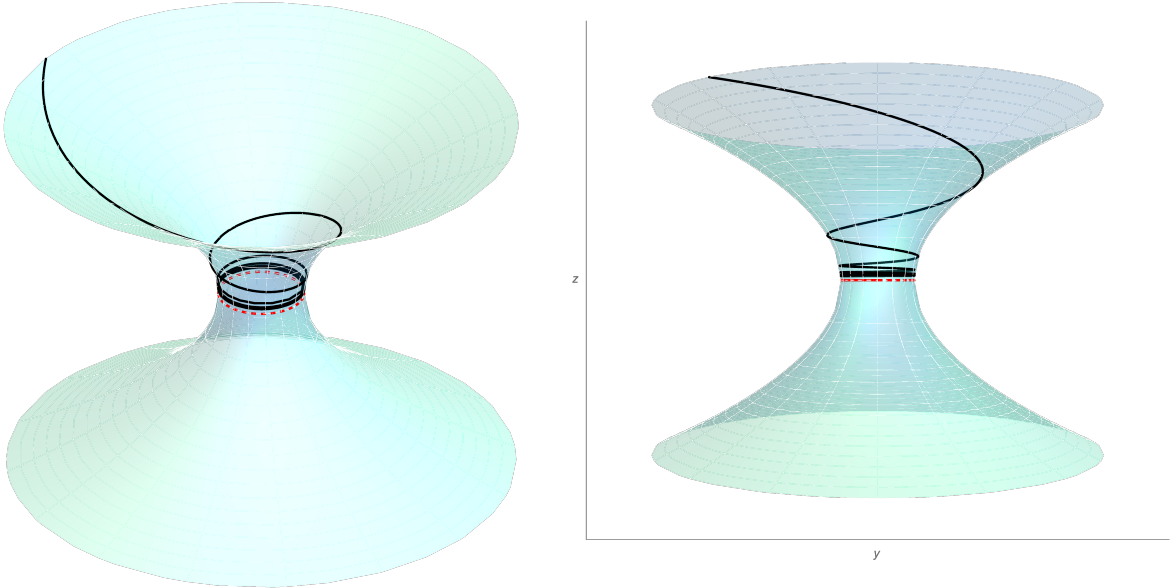


FIG. 8. Embedding diagram onto which the particle trajectory is projected. The particle with the parameters at the black point in column (a) of Fig. 1, giving $r_{\text{th}} = r_{m3} = r_{m2}$, begins at spatial infinity and travels toward the triple root radius at the throat.

When the particle approaches the throat at the triple root, $\phi^B \sim (r - r_{\text{th}})^{-1/2}$ and $t^B \sim (r - r_{\text{th}})^{-1/2}$ in (38) and (39) due to the divergence of $H(\psi^B(r)|k^B)$ as $r \rightarrow r_{\text{th}}$, which shows a stronger power-law divergence than the logarithmic divergence in the case of the throat at the double root.

C. $r_{m2} = r_{m3} < r_{th}$

Another unique trajectory in wormhole spacetimes is that the particle traverses the throat and moves from one asymptotically flat region to the other via the throat. The corresponding parameters are at the blue point in column (b) of Fig. 1. In this case, the double root $r_{m3} = r_{m2} = r_{m_{cu}}$ is considered and the radius of the throat is larger than the double root ($r_{m_{cu}} < r_{th}$). The solutions are obtained as

$$\phi^C(r) = \nu_{r_i} \frac{2\lambda_m}{\sqrt{(\gamma_m^2 - 1)(2M - r_{m1})r_{th}}} \left[\frac{r_{th} - 2M}{r_{th} - r_{m_{cu}}} \Pi(\alpha^C; \psi^C(r)|k^C) \right] - \phi_i^C, \quad (42)$$

$$\begin{aligned} t^C(r) = & \nu_{r_i} \frac{\gamma_m}{\sqrt{\gamma_m^2 - 1}} \left\{ \sqrt{\frac{(r - r_{th})(r - r_{m1})r}{r - 2M}} + \frac{1}{\sqrt{(2M - r_{m1})r_{th}}} \left[(r_{m1} - 2M)r_{th} E(\psi^C(r)|k^C) \right. \right. \\ & + \frac{8M^3 + r_{m_{cu}}r_{m1}r_{th} + 4M^2(r_{m1} + r_{th} + r_{m_{cu}}) - 2M[r_{m1}r_{th} + r_{m_{cu}}(r_{m1} + r_{th})]}{2M - r_{m_{cu}}} F(\psi^C(r)|k^C) \\ & \left. \left. + (r_{th} - 2M)(2M + r_{m1} + r_{th} + 2r_{m_{cu}}) \Pi(\beta^C; \psi^C(r)|k^C) + \frac{2r_{m_{cu}}^3(2M - r_{th})}{(2M - r_{m_{cu}})(r_{th} - r_{m_{cu}})} \Pi(\alpha^C; \psi^C(r)|k^C) \right] \right\} - t_i^C, \quad (43) \end{aligned}$$

where

$$\begin{aligned} \psi^C(r) &= \sin^{-1} \sqrt{\frac{(r - r_{th})(2M - r_{m1})}{(r - 2M)(r_{th} - r_{m1})}}; & k^C &= \frac{2M(r_{th} - r_{m1})}{r_{th}(2M - r_{m1})}; & \nu_{r_i} &= -1; \\ \alpha^C &= \frac{(r_{th} - r_{m1})(r_{m_{cu}} - 2M)}{(2M - r_{m1})(r_{m_{cu}} - r_{th})}; & \beta^C &= \frac{r_{th} - r_{m1}}{2M - r_{m1}}. \end{aligned} \quad (44)$$

An illustrative plot is shown in Fig. 9.

We can examine the evolution of the azimuthal angle ϕ and the time t to understand how the particle crosses the throat. This gives $\phi^C(r) \sim (r - r_{th})^{1/2} + \phi^C(r_{th})$ and $t^C(r) \sim (r - r_{th})^{1/2} + t^C(r_{th})$ from (42) and (43). Thus, as the particle traverses the wormhole, $\phi(r)$ and $t(r)$ change continuously.

Here we speculate about the gravitational waveforms generated by these orbits. As the particle spirals toward the throat at the double or triple roots along an orbital path, gravitational waves with a chirp-type waveform are expected to be generated. Since there are no triple roots associated with the radial potential for unbound motion in a typical black hole [31], in wormhole spacetimes the resulting waveform could have a larger amplitude and a higher oscillation frequency than the waveform due to double roots. The most interesting scenario is that the throat is a simple root. In this case, the particle passes smoothly

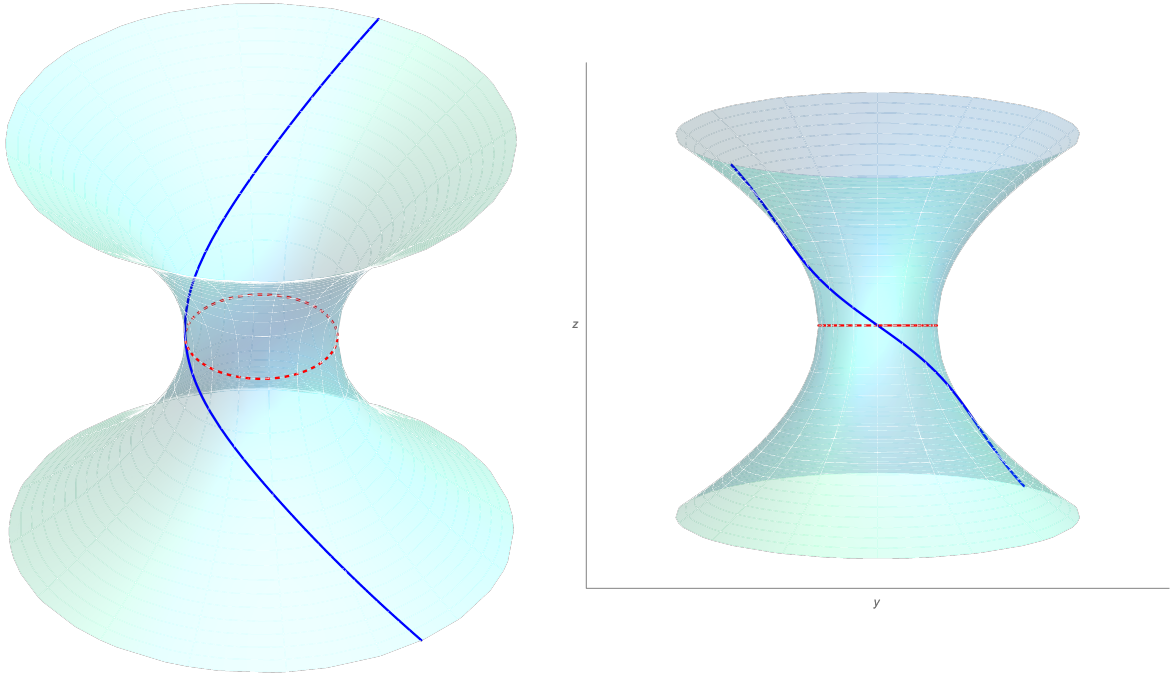


FIG. 9. Embedding diagram onto which the particle trajectory is projected. The particle with the parameters at the blue point in column (b) of Fig. 1, giving $r_{m2} = r_{m3} < r_{\text{th}}$, starts at spatial infinity and travels directly through the throat to another spacetime region.

through the throat and travels from one spacetime region to another [39, 40]. In Fig. 9, in one region of spacetime, the particle plunges towards the throat. The gravitational waves are generated in the form of a pulse. Later, the particle crosses the throat into another region of spacetime, where local ripples in spacetime can no longer travel back through the throat to this region. This creates a distinct gap in the signal. In the other region, the particles emerge from the throat, generating gravitational waves in the form of another pulse. Therefore, these waveforms could represent distinct signatures of gravitational waves generated when astrophysical objects plunge into or emerge from wormholes.

D. Homoclinic orbit

We now consider one of the most interesting trajectories in the bound motion with $\gamma_m^2 < 1$, namely the homoclinic orbit. Such an orbit acts as a separatrix between bound and plunging geodesics, approaching an energetically bound yet unstable circular orbit with

the parameters at the double root. As compared with the homoclinic orbit in black holes [32, 37], the unique feature of wormholes is that the unstable double root is located at the throat. This gives rise to a throat-induced homoclinic orbit. In Fig. 3, the purple point in column (a2) represents the parameters of the double root at the throat, $r_{\text{th}} = r_{m2}$. From the corresponding effective potentials in Fig. 4, the particle starts from the largest root $r_i \lesssim r_{m3}$ and spends an infinite amount of time reaching the unstable circular orbit with the radius $r_{\text{th}} = r_{m2}$. The analytical solution for a homoclinic orbit can be expressed as follows

$$\phi^D(r) = \nu_{r_i} \frac{2\lambda_m}{\sqrt{(1-\gamma_m^2)(r_{m3}-2M)r_{m1}}} \left[-\frac{2M}{r_{\text{th}}} F(\psi^D(r)|k^D) + \frac{r_{m3}(r_{\text{th}}-2M)}{r_{\text{th}}(r_{\text{th}}-r_{m3})} \Pi(\alpha^D; \psi^D(r)|k^D) \right] - \phi_i^D, \quad (45)$$

$$t^D(r) = -\nu_{r_i} \frac{\gamma_m}{\sqrt{1-\gamma_m^2}} \left\{ \sqrt{\frac{(r-2M)(r_{m3}-r)(r-r_{m1})}{r}} \right. \\ \left. + \frac{1}{\sqrt{(r_{m3}-2M)r_{m1}}} \left[(r_{m3}-2M)r_{m1}E(\psi^D(r)|k^D) - r_{m1}r_{m3}F(\psi^D(r)|k^D) \right] \right. \\ \left. + (2M+r_{m1}+r_{m3}+2r_{\text{th}})r_{m3}\Pi(\beta^D; \psi^D(r)|k^D) + \frac{2r_{\text{th}}^2 r_{m3}}{r_{m3}-r_{\text{th}}}\Pi(\alpha^D; \psi^D(r)|k^D) \right\} - t_i^D \quad (46)$$

with $\nu_{r_i} = -1$, where

$$\psi^D(r) = \sin^{-1} \sqrt{\frac{(r-r_{m3})r_{m1}}{r(r_{m1}-r_{m3})}}; \quad k^D = \frac{2M(r_{m3}-r_{m1})}{r_{m1}(r_{m3}-2M)}; \\ \alpha^D = \frac{r_{\text{th}}(r_{m1}-r_{m3})}{(r_{\text{th}}-r_{m3})r_{m1}}; \quad \beta^D = \frac{r_{m1}-r_{m3}}{r_{m1}}. \quad (47)$$

The additional root at the throat of the radial potential in (14) for $\lambda \neq 0$ renders the solution being more complicated than that of the black hole for $\lambda = 0$ in terms of the elementary functions [32]. Figure 10 illustrates this orbit with the solution given above, where the parameters of the plot correspond to the purple point in column (a2) of Fig. 3.

In the limit of $r \rightarrow r_{\text{th}} + \varepsilon$, Eqs. (45) and (46) exhibit a logarithmic divergence when approaching the double root due to the elliptic integral Π [32]. Following [43], the Lyapunov exponent can be related to the inverse of the time scale of instability that characterizes the orbital motion. To proceed, we introduce the effective potential in terms of the coordinate time t , derived from the equations of motion (8) and (10) as

$$\frac{1}{2} \left(\frac{dr}{dt} \right)^2 + \mathcal{V}_{\text{eff}}(r) = 0, \quad (48)$$

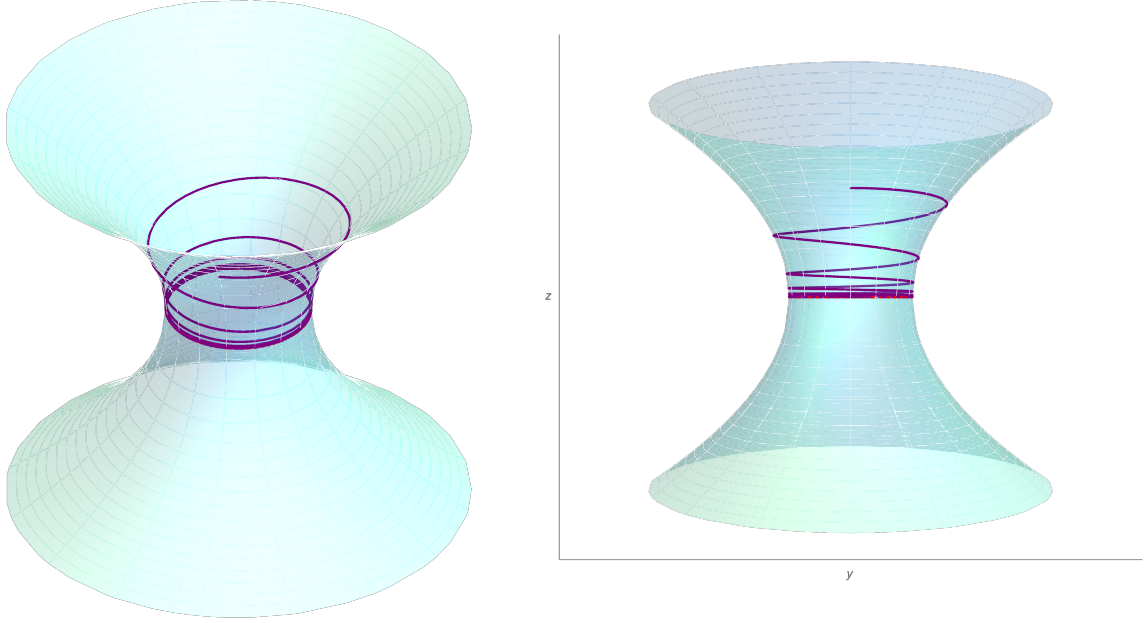


FIG. 10. Embedding diagram onto which the particle's homoclinic orbit is projected. The particle has the parameters corresponding to the purple point in column (a2) of Fig. 3. Here, the particle begins at the largest root $r_i \lesssim r_{m3}$, and subsequently moves toward the unstable circular orbit with the radius $r_{m2} = r_{\text{th}}$, associated with the double root of the radial potential.

where

$$\mathcal{V}_{\text{eff}}(r) = -\frac{(\gamma_m^2 - 1)(r - r_{m1})(r - r_{\text{th}})(r - r_{\text{th}})(r - r_{m3})(r - 2M)}{2r^5\gamma_m^2}. \quad (49)$$

Next, we consider the particle located near the unstable double root of $\mathcal{V}_{\text{eff}}(r)$, which means that $r(t) = r_{\text{th}} + \varepsilon(t)$. This leads to the solution $r(t) - r_{\text{th}} \approx \varepsilon(0)e^{\Lambda t}$ with the Lyapunov exponent Λ determined by

$$\Lambda^2 = -\partial_r^2 \mathcal{V}_{\text{eff}}(r) \Big|_{r=r_{\text{th}}} = \frac{(\gamma_m^2 - 1)(r_{\text{th}} - r_{m1})(r_{\text{th}} - r_{m3})(r_{\text{th}} - 2M)}{2r_{\text{th}}^5\gamma_m^2}. \quad (50)$$

According to the above formulas, Fig. 11(a) illustrates the Lyapunov exponent as a function of γ_m for a fixed r_{th} . As γ_m , whose range is given by (31), increases towards $\gamma_m = 1$, the Lyapunov exponent grows to its maximum value. The Lyapunov exponent is plotted against r_{th} for a fixed γ_m in panel (b), showing a maximum value of Λ^2 with a particular value of r_{th} . To find the corresponding r_{th} for a fixed γ_m analytically, the condition $\frac{d}{dr_{\text{th}}}\Lambda^2 = 0$ is implemented with the roots r_{m1} and r_{m3} , which are functions of $\lambda_m = \lambda_m(r_{\text{th}})$ in (28). In

Appendix B and with the Vieta's formulas, where $r_{m1} + r_{m3} = -\frac{2M}{\gamma_m^2 - 1} - r_{\text{th}}$ and $r_{m1}r_{m3} = -\frac{2M\lambda_m^2}{(\gamma_m^2 - 1)r_{\text{th}}}$, the value of r_{th} giving the maximum Lyapunov exponent is given by

$$r_{\text{th}}(\gamma_m) = \frac{3M(3\gamma_m^2 - 4) + M\sqrt{(81\gamma_m^4 - 88\gamma_m^2 + 16)}}{4(\gamma_m^2 - 1)}, \quad (51)$$

showing r_{th} as a function of γ_m in the main figure of Fig. 11(c). The inset of Fig. 11(c) is to display the corresponding Lyapunov exponent with the values of γ_m and r_{th} satisfying (51). As the value of γ_m increases, leading to a smaller r_{th} , the Lyapunov exponent is expected to increase. In the limit $\gamma_m \rightarrow 1$, the radius r_{th} approaches to $16M/3$ from (51), and the

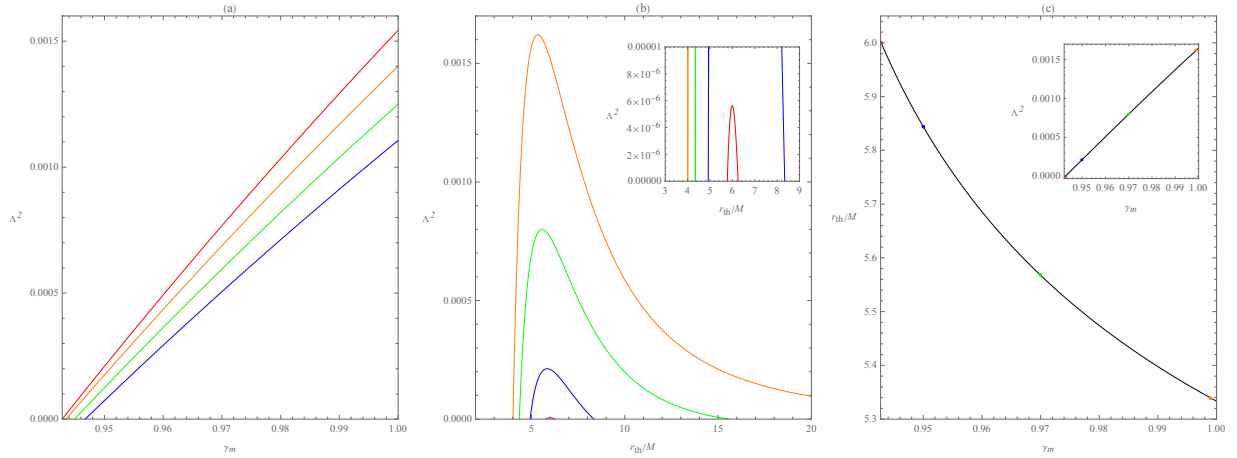


FIG. 11. The Lyapunov exponent as a function of the throat radius r_{th} and particle energy γ_m : (a) shows the Lyapunov exponent as a function of γ_m for different wormhole parameters, that is $r_{\text{th}} = 6M$ (red), $r_{\text{th}} = 6.5M$ (orange), $r_{\text{th}} = 7M$ (green), $r_{\text{th}} = 7.5M$ (blue), where the similar figure is seen in Fig. 8 in [34]; (b) shows the Lyapunov exponent as a function of r_{th} for different particle energies: $\gamma_m = 0.943$ (red), $\gamma_m = 0.95$ (blue), $\gamma_m = 0.97$ (green) and $\gamma_m = 0.999$ (orange); (c) considers the maximum value of the Lyapunov exponent in (b), and then obtains the relation $r_{\text{th}}(\gamma_m)$ in (51).

associated Lyapunov exponent Λ^2 can be achieved by the value of $27/16384M^2$ from (50). As compared with Schwarzschild black holes, one can consider the unstable radius r_{mcu} given by the double root at $r_{m3} = r_{m2}$, and in the limit of $\gamma_m \rightarrow 1$, the unstable radius can be $r_{\text{mcu}} = 4M$ in Fig. 6 with the Lyapunov exponent $\Lambda^2 = 1/128M^2$, which is less than the bound of $\Lambda \leq 2\pi k_B T$ with its value of $\Lambda^2 \leq 1/16M^2$ due to the black hole temperature $k_B T = (8\pi M)^{-1}$. With $\gamma_m = 1$, the throat radius at the double root in a DS wormhole,

giving the maximum value of the Lyapunov exponent is larger than the radius of the unstable circular motion in a Schwarzschild black hole. In this case, therefore, the Lyapunov exponent of an DS wormhole is typically smaller than that of a Schwarzschild black hole.

E. Inspiral through throat

Another unique bound orbit is to consider the parameters at the triple roots ($r_{\text{th}} < r_{m3} = r_{m2} = r_{m1} = 6M$) with $\gamma_m = 2\sqrt{2}/3$, where a DS wormhole has the radius of the ISCO of $6M$. Following the dark blue point in column (b1) of Fig. 3, the particle starts from r_i slightly smaller than the radius of the ISCO but larger than the throat radius r_{th} , i.e. $r_{\text{th}} < r_i \lesssim 6M$. According to the effective potentials in Fig. 5, the particle will inspiral from near the ISCO radius, plunge into the wormhole throat, and reach the other spacetime region. It will then bounce back and forth between these two regions via the wormhole. This is a unique feature of the particle orbits in wormhole spacetimes. The solution can be represented as

$$\begin{aligned} \phi^E(r) = & \nu_{r_i} \frac{2\lambda_m}{\sqrt{1-\gamma_m^2}} \left[\frac{r_{\text{th}} - 2M}{(6M - r_{\text{th}})\sqrt{4Mr_{\text{th}}}} F(\psi_\phi^E(r)|k_\phi^E) - \frac{\sqrt{4Mr_{\text{th}}}}{6M(6M - r_{\text{th}})} E(\psi_\phi^E(r)|k_\phi^E) \right. \\ & \left. - \frac{4M}{6M(6M - r_{\text{th}})} \sqrt{\frac{(r - r_{\text{th}})r}{(6M - r)(r - 2M)}} \right] - \phi_i^E, \end{aligned} \quad (52)$$

where

$$\psi_\phi^E(r) = \sin^{-1} \sqrt{\frac{4M(r - r_{\text{th}})}{(r - 2M)(6M - r_{\text{th}})}}; \quad k_\phi^E = \frac{2M(6M - r_{\text{th}})}{4Mr_{\text{th}}}; \quad \nu_{r_i} = -1. \quad (53)$$

And,

$$\begin{aligned} t^E(r) = & \nu_{r_i} \frac{\gamma_m}{\sqrt{1-\gamma_m^2}} \frac{1}{(2M - 6M)(6M - r_{\text{th}})} \left\{ -72M^2 \sqrt{\frac{r(r - 2M)(r - r_{\text{th}})}{6M - r}} + \frac{1}{\sqrt{6M(r_{\text{th}} - 2M)}} \right. \\ & \times \left[(12M^2 - 2Mr_{\text{th}} - 108M^2 + 6Mr_{\text{th}}) \sqrt{\frac{6M(6M - r)(r - r_{\text{th}})(r_{\text{th}} - 2M)(r - 2M)}{r}} \right. \\ & + 24M^2(2M - r_{\text{th}})(r_{\text{th}} - 24M) E(\psi_t^E(r)|k_t^E) - 24M^2 r_{\text{th}}(18M - r_{\text{th}}) F(\psi_t^E(r)|k_t^E) \\ & \left. \left. - 4Mr_{\text{th}}(r_{\text{th}} - 6M)(20M + r_{\text{th}}) \Pi(\alpha_t^E; \psi_t^E(r)|k_t^E) \right] \right\} - t_i^E, \end{aligned} \quad (54)$$

where

$$\psi_t^E(r) = \sin^{-1} \sqrt{\frac{6M(r - r_{\text{th}})}{r(6M - r_{\text{th}})}}; \quad k_t^E = \frac{2M(6M - r_{\text{th}})}{6M(2M - r_{\text{th}})}; \quad \alpha_t^E = 1 - \frac{r_{\text{th}}}{6M}. \quad (55)$$

Note that the expressions of analytical solutions are not unique. Here we just choose one of them. The trajectory is shown in Fig. 12.

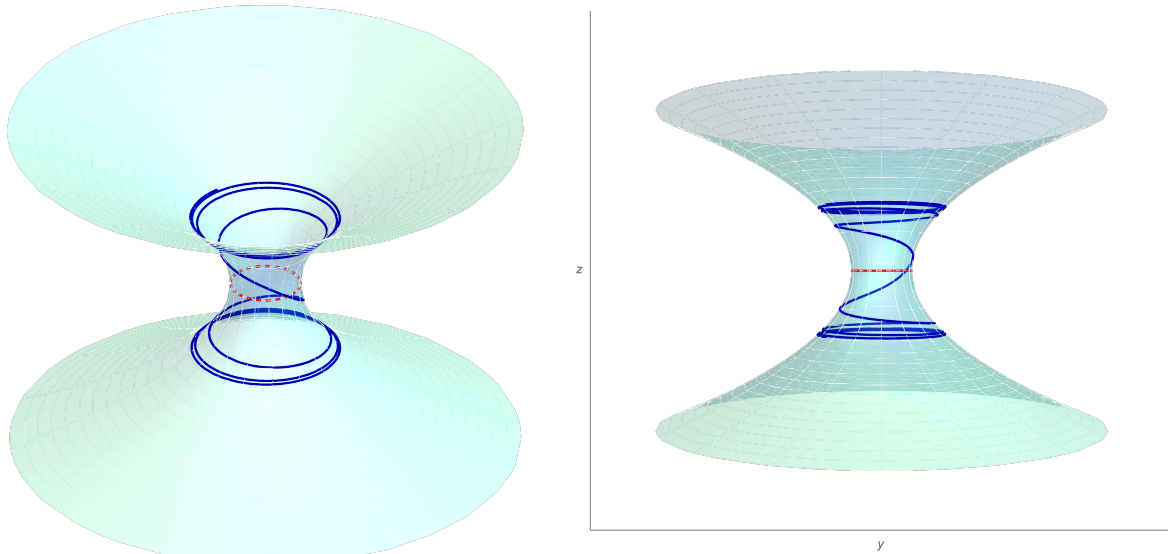


FIG. 12. Embedding diagram onto which the particle’s inspiral orbit is projected. With the parameters at the dark blue point in column (b1) of Fig. 3, the particle starting at $r_{\text{th}} < r_i \lesssim r_{\text{isco}}$ inspirals from near the ISCO radius, plunges into the wormhole throat, and reaches another spacetime region. It will then bounce back and forth between the two spacetime regions connected by the wormhole.

When $r \rightarrow r_{\text{th}}$, $\phi^E(r)$ and $t^E(r)$ become finite since $\phi^E(r) \sim (r - r_{\text{th}})^{1/2} + \phi^E(r_{\text{th}})$ and $t^E(r) \sim (r - r_{\text{th}})^{1/2} + t^E(r_{\text{th}})$ from (52) and (54). This is the same as the case in Sec. IV C, where the particle also crosses the throat smoothly and enters another spacetime region. Moreover, as taking the limit of $r_{\text{th}} \rightarrow 2M$ (the event horizon of a Schwarzschild black hole), the orbital solutions reduce to those of black holes in [33]. Around the black hole, although $\phi(r)$ changes smoothly across the horizon, $t(r)$ diverges as $t(r) \sim \log(r - 2M)$ in [33]. According to Fig. 12, the implications of these orbits in the generation of gravitational waves are discussed [39, 40]. In one spacetime region, the inbound particle shrinks its orbital radius toward the throat, generating gravitational waves in the form of a standard chirp. The particle then crosses the throat into another region of spacetime, creating a distinct gap in a signal. In the other region, the outbound particle spirals outward, generating gravitational

waves in the form of an antichirp. Thus, antichirps and gaps in gravitational waveforms could be distinct signatures of the gravitational waves generated by astrophysical objects spiraling in and out of wormholes.

V. SUMMARY AND OUTLOOK

In this paper, we examine the motion of particles around Damour-Solodukhin wormholes, which are Schwarzschild-like wormholes with an additional parameter λ that determines the radius of the throat r_{th} . To our knowledge, it is for the first time to derive analytical solutions for some unique orbits in DS wormhole spacetimes, which also exist in other wormhole spacetimes. We compare these trajectories around DS wormholes with those around Schwarzschild black holes, for which $\lambda = 0$. The corresponding radial potential is derived from timelike geodesics with four non-zero roots. Three of these roots ($r_{m1} \leq r_{m2} \leq r_{m3}$ if they are all real) depend on the mass of the wormhole and two constants of motion: energy and angular momentum per unit particle's mass (γ_m, λ_m). The additional root is at the throat. We classify the roots and construct the parameter space diagram in terms of λ_m and the throat radius r_{th} , considering various values of γ_m for the bound and unbound motion. In this context, the throat, together with the other roots, can become double, triple, and quartic roots. In particular, triple roots are associated with the radius of the ISCO, which may in principle be observationally accessible. One of the main conclusions is that wormhole spacetimes can potentially be distinguished from black hole spacetimes by the radius of the ISCO at the throat, which can be observed from the signature of the iron line profile [18]. This occurs as long as $r_{\text{th}} > 6M$ and the triple root $r_t = r_{\text{th}} = r_{m3} = r_{m2}$ is reached for a specific set of parameters. When $r_{\text{th}} < 6M$, the throat lies behind the triple root $r_{m1} = r_{m2} = r_{m3}$, which is also the triple root of black holes with $\lambda = 0$. In this case, the radius of the ISCO of the wormhole is the same as that of the black hole, and the two cannot be distinguished from each other. At $r_{\text{th}} = r_{m1} = r_{m2} = r_{m3} = 6M$, the root is quartic.

We derive closed-form orbital solutions for the bound or unbound motion. In unbound motion, when the particle starts from spatial infinity and travels towards the throat, we find that, when the double root (or triple) is at the throat $r_{\text{th}} = r_{m3}$ (or $r_{\text{th}} = r_{m2} = r_{m3}$), the azimuthal angle $\phi(r)$ and the coordinate time $t(r)$ exhibit the divergence $\log(r - r_{\text{th}})$ (or

$(r - r_{\text{th}})^{-1/2}$) as $r \rightarrow r_{\text{th}}$. Conversely, when the throat radius is a single root, i.e. $r_{m2} = r_{m3} < r_{\text{th}}$, $\phi(r)$ and $t(r)$ change smoothly across the throat in a way of $\phi(r) \sim (r - r_{\text{th}})^{1/2} + \phi(r_{\text{th}})$ and $t(r) \sim (r - r_{\text{th}})^{1/2} + t(r_{\text{th}})$ as $r \rightarrow r_{\text{th}}$. The orbits passing through the wormhole throat could generate a unique pulse-gap signature of the gravitational waveforms that could be observed [39, 40].

Later, we derive exact homoclinic solutions in bound motion. One notable feature is the throat-homoclinic configuration, in which the unstable circular orbit is located at $r_{m2} = r_{\text{th}}$. The closed-form solutions of $\phi(r)$ and $t(r)$ demonstrate that the third-kind elliptic integral, Π , determines how a particle approaches the throat, exhibiting divergent behavior as r approaches r_{th} in the form of $\log(r - r_{\text{th}})$. The corresponding Lyapunov exponent is calculated, showing that the maximum exponent value is $27/16384M^2$ when $r_{\text{th}} = 16M/3$ and $\gamma_m \rightarrow 1$. Once a homoclinic orbit exists, small perturbations, such as random kicks, are expected to induce chaos. Our closed-form solution provides the basis for constructing Melnikov functions [44], where the simple zeros of the Melnikov function imply chaotic dynamics. We also analyze inspiral orbits with parameters $r_{\text{th}} < r_{m1} = r_{m2} = r_{m3} = 6M$, originating near the triple roots at $6M$ and subsequently plunging into the throat. The particle bounces back and forth between the two spacetime regions connected by the wormhole multiple times. The spiral motions into and out of the wormhole are of astrophysical interest because they are directly related to the generation of gravitational waves exhibiting a typical chirp-gap-antichirp pattern [39, 40]. These analytical orbital solutions could be useful for analyzing this unique waveform, which deserves further investigation.

Appendix A: Embedding Diagrams of DS wormhole

Following [11], we construct the embedding diagram to represent the DS wormhole that connects two different asymptotically flat regions. Considering a slice in the plane of $\theta = \pi/2$, the metric in (3) at a fixed moment ($t = \text{constant}$) is

$$ds^2 = \frac{dr^2}{g(r)} + r^2 d\phi^2 \quad (\text{A1})$$

with $g(r) = 1 - \frac{2M(1+\lambda^2)}{r}$. We embed the metric into a three-dimensional Euclidean space to illustrate the slice. The spacetime metric can be expressed in cylindrical coordinates as

$$ds^2 = d\rho^2 + \rho^2 d\phi^2 + dz^2 = \left[\left(\frac{d\rho}{dr} \right)^2 + \left(\frac{dz}{dr} \right)^2 \right] dr^2 + \rho^2 d\phi^2. \quad (\text{A2})$$

With the condition $\rho = r$, the combination of (A1) and (A2) yields the equation for the embedding surface, which is given by

$$\frac{dz}{dr} = \pm \sqrt{\frac{r}{r - 2M(1 + \lambda^2)} - 1}. \quad (\text{A3})$$

Integrating it into r results in

$$z = \pm \sqrt{8M(1 + \lambda^2)[r - 2M(1 + \lambda^2)]}. \quad (\text{A4})$$

Appendix B: Roots of the radial potential $R_m(r)$

The radial potential $R_m(r)$ (12) can be expressed as

$$R_m(r) = r P_m(r), \quad P_m(r) = Ar^3 + Br^2 + Cr + D, \quad (\text{B1})$$

where the coefficients are written in terms of the parameter M and the constants of motion, γ_m, λ_m as

$$A = \gamma_m^2 - 1, \quad (\text{B2})$$

$$B = 2M, \quad (\text{B3})$$

$$C = -\lambda_m^2, \quad (\text{B4})$$

$$D = 2M\lambda_m^2. \quad (\text{B5})$$

We denote the roots of $P_m(r)$ as $P_m(r) = (\gamma_m^2 - 1)(r - r_{m1})(r - r_{m2})(r - r_{m3})$, with the order of $r_{m3} > r_{m2} > r_{m1}$ when they are all real. The roots solutions are

$$r_{m1} = -\frac{2M}{3(\gamma_m^2 - 1)} + X_m + Y_m, \quad (\text{B6})$$

$$r_{m2} = -\frac{2M}{3(\gamma_m^2 - 1)} + e^{-2\pi i/3} X_m + e^{2\pi i/3} Y_m, \quad (\text{B7})$$

$$r_{m3} = -\frac{2M}{3(\gamma_m^2 - 1)} + e^{2\pi i/3} X_m + e^{-2\pi i/3} Y_m, \quad (\text{B8})$$

where

$$X_m = \sqrt[3]{-\frac{q_m}{2} + \sqrt{\Delta_C}}, \quad Y_m = \sqrt[3]{-\frac{q_m}{2} - \sqrt{\Delta_C}}, \quad \Delta_C = \left(\frac{q_m}{2}\right)^2 + \left(\frac{p_m}{3}\right)^3, \quad (\text{B9})$$

and p_m and q_m are the short notation for

$$p_m = \frac{3AC - B^2}{3A^2}, \quad (\text{B10})$$

$$q_m = \frac{27A^2D - 9ABC + 2B^3}{27A^3}. \quad (\text{B11})$$

Notice that $r_{m1} + r_{m2} + r_{m3} = -\frac{2M}{\gamma_m^2 - 1}$. The formula shows that when $\Delta_C > 0$, there is one real root (r_{m1}) and a pair of complex conjugate roots ($r_{m2} = r_{m3}^*$); when $\Delta_C = 0$, there is at least one multiple root; and when $\Delta_C < 0$, there are three distinct real roots. Moreover, $r_{m1} < 0$ if $\gamma_m^2 > 1$, and $r_{m1} > 0$ if $\gamma_m^2 < 1$.

Appendix C: Elliptic Integrals

The incomplete elliptic integrals of the first, second, and third kinds are defined as

$$\begin{aligned} F(\varphi|k) &\equiv \int_0^\varphi \frac{d\vartheta}{\sqrt{1 - k \sin^2 \vartheta}}, \\ E(\varphi|k) &\equiv \int_0^\varphi \sqrt{1 - k \sin^2 \vartheta} d\vartheta, \\ \Pi(\alpha; \varphi|k) &\equiv \int_0^\varphi \frac{d\vartheta}{(1 - \alpha \sin^2 \vartheta) \sqrt{1 - k \sin^2 \vartheta}}, \end{aligned} \quad (\text{C1})$$

where they will become the complete ones as $\varphi = \pi/2$.

In Sec. [IV B](#), we use the behavior

$$\Pi(\alpha; \varphi|k) = -\frac{H(\varphi|k)}{\alpha} + \mathcal{O}\left(\frac{1}{\alpha^2}\right) \quad (\text{C2})$$

in the limit $\alpha \rightarrow \infty$, where

$$H(\varphi|k) = \int_0^\varphi \frac{d\vartheta}{\sin^2 \vartheta \sqrt{1 - k \sin^2 \vartheta}}. \quad (\text{C3})$$

ACKNOWLEDGMENTS

This work was supported in part by the National Science and Technology Council (NSTC) of Taiwan, Republic of China.

- [1] A. Einstein and N. Rosen, The particle problem in the general theory of relativity, *Phys. Rev.* **48**, 73 (1935).
- [2] M. S. Morris, K. S. Thorne, and U. Yurtsever, Wormholes, time machines, and the weak energy condition, *Phys. Rev. Lett.* **61**, 1446 (1988).
- [3] M. Visser, *Lorentzian Wormholes* (American Institute of Physics, New York, 1995).
- [4] T. Damour and S. N. Solodukhin, Wormholes as black hole foils, *Phys. Rev. D* **76**, 024016 (2007).
- [5] The Event Horizon Telescope Collaboration, First M87 Event Horizon Telescope results. I. The shadow of the supermassive black hole, *Astrophys. J. Lett.* **875**, L1 (2019).
- [6] The Event Horizon Telescope Collaboration, First Sagittarius A* Event Horizon Telescope results. I. The shadow of the supermassive black hole in the center of the Milky Way, *Astrophys. J. Lett.* **930**, L12 (2022).
- [7] P. Bueno, P. A. Cano, F. Goelen, T. Hertog, and B. Vercknocke, Echoes of Kerr-like wormholes, *Phys. Rev. D* **97**, 024040 (2018).
- [8] V. Cardoso, E. Franzin, and P. Pani, Is the Gravitational-Wave Ringdown a Probe of the Event Horizon?, *Phys. Rev. Lett.* **116**, 171101 (2016).
- [9] R. Konoplya, How to tell the shape of a wormhole by its quasinormal modes, *Phys. Lett. B* **784**, 43 (2018).
- [10] S. Kasuya and M. Kobayashi, Throat effects on shadows of Kerr-like wormholes, *Phys. Rev. D* **103**, 104050 (2021).
- [11] M. Amir, K. Jusufi, A. Banerjee, and S. Hansraj, Shadow images of Kerr-like wormholes, *Classical Quantum Gravity* **36**, 215007 (2019).
- [12] N. Tsukamoto, Nonlogarithmic divergence of a deflection angle by a marginally unstable photon sphere of the Damour-Solodukhin wormhole in a strong deflection limit, *Phys. Rev. D* **101**, 104021 (2020).

- [13] A. Övgün, Light deflection by Damour-Solodukhin wormholes and Gauss-Bonnet theorem, *Phys. Rev. D* **98**, 044033 (2018).
- [14] R. Shaikh, Shadows of rotating wormholes, *Phys. Rev. D* **98**, 024044 (2018).
- [15] P. G. Nedkova, V. K. Tinchev, and S. S. Yazadjiev, Shadow of a rotating traversable wormhole, *Phys. Rev. D* **88**, 124019 (2013).
- [16] T. Hsieh, D.-S. Lee, and C.-Y. Lin, Throat effects on strong gravitational lensing in Kerr-like wormholes, *Phys. Rev. D* **111**, 044051 (2025).
- [17] D.-C. Dai and D. Stojkovic, Observing a wormhole, *Phys. Rev. D* **100**, 083513 (2019).
- [18] C. Liu, H. Siew, H.-X. Jiang, Y. Mizuno, and T. Zhu, Signature of iron line profile from a Kerr-like wormhole, *A&A* [10.1051/0004-6361/202557027](https://doi.org/10.1051/0004-6361/202557027) (2026).
- [19] B. P. Abbott *et al.* (LIGO Scientific and Virgo Collaboration), Observation of Gravitational Waves from a Binary Black Hole Merger, *Phys. Rev. Lett.* **116**, 061102 (2016).
- [20] B. P. Abbott *et al.* (LIGO Scientific and Virgo Collaboration), GWTC-1: A Gravitational-Wave Transient Catalog of Compact Binary Mergers Observed by LIGO and Virgo during the First and Second Observing Runs, *Phys. Rev. X* **9**, 031040 (2019).
- [21] R. Abbott *et al.* (LIGO Scientific and Virgo Collaboration), GWTC-2: Compact Binary Coalescences Observed by LIGO and Virgo during the First Half of the Third Observing Run, *Phys. Rev. X* **11**, 021053 (2021).
- [22] E. Consortium *et al.*, The gravitational universe, arXiv: 1305.5720 [10.48550/arxiv.1305.5720](https://doi.org/10.48550/arxiv.1305.5720) (2013).
- [23] E. Barausse *et al.*, Prospects for fundamental physics with LISA, *Gen. Relativ. Gravit.* **52** (2020).
- [24] LISA Consortium Waveform Working Group, Waveform modelling for the Laser Interferometer Space Antenna, *Living Reviews in Relativity* **28**, 9 (2025).
- [25] S. Babak, J. Gair, A. Sesana, E. Barausse, C. F. Sopuerta, C. P. L. Berry, E. Berti, P. Amaro-Seoane, A. Petiteau, and A. Klein, Science with the space-based interferometer LISA. V. Extreme mass-ratio inspirals, *Phys. Rev. D* **95**, 103012 (2017).
- [26] B. Kocsis, N. Yunes, and A. Loeb, Observable signatures of extreme mass-ratio inspiral black hole binaries embedded in thin accretion disks, *Phys. Rev. D* **84**, 024032 (2011).
- [27] C. A. Benavides-Gallego, W.-B. Han, D. Malafarina, B. Ahmedov, and A. Abdujabbarov, Spinning test particle motion around a traversable wormhole, *Phys. Rev. D* **104**, 084024

- (2021).
- [28] B. Narzilloev, D. Malafarina, A. Abdujabbarov, B. Ahmedov, and C. Bambi, Particle motion around a static axially symmetric wormhole, *Phys. Rev. D* **104**, 064016 (2021).
 - [29] F. Abdulxamidov, C. A. Benavides-Gallego, W.-B. Han, J. Rayimbaev, and A. Abdujabbarov, Spinning test particle motion around a rotating wormhole, *Phys. Rev. D* **106**, 024012 (2022).
 - [30] C.-Y. Liu, D.-S. Lee, and C.-Y. Lin, Geodesic motion of neutral particles around a Kerr–Newman black hole, *Classical Quantum Gravity* **34**, 235008 (2017).
 - [31] C.-Y. Wang, D.-S. Lee, and C.-Y. Lin, Null and timelike geodesics in the Kerr–Newman black hole exterior, *Phys. Rev. D* **106**, 084048 (2022).
 - [32] Y.-T. Li, C.-Y. Wang, D.-S. Lee, and C.-Y. Lin, Homoclinic orbits in Kerr–Newman black holes, *Phys. Rev. D* **108**, 044010 (2023).
 - [33] Y.-C. Ko, D.-S. Lee, and C.-Y. Lin, Inspiral and plunging orbits in Kerr–Newman spacetimes, *Phys. Rev. D* **109**, 084043 (2024).
 - [34] S.-Y. Ciou, T. Hsieh, and D.-S. Lee, Dynamics of spinning particles in Reissner–Nordström black hole exterior, *JCAP* **05** (2025), 086.
 - [35] Y.-P. Chen, T. Hsieh, and D.-S. Lee, Motion of spinning particles in the Kerr–Newman black hole exterior. I. Periodic orbits, arXiv: 2510.05603 [10.48550/arxiv.2510.05603](https://arxiv.org/abs/2510.05603) (2025).
 - [36] J. B. Hartle, Gravity: An Introduction to Einstein’s General Relativity (Benjamin Cummings, New York, 2003).
 - [37] J. Levin and G. Perez-Giz, Homoclinic orbits around spinning black holes. I. Exact solution for the Kerr separatrix, *Phys. Rev. D* **79**, 124013 (2009).
 - [38] J. Maldacena, S. H. Shenker, and D. Stanford, A bound on chaos, *J. High Energy Phys.* **08** (2016), 106.
 - [39] J. B. Dent, W. E. Gabella, K. Holley-Bockelmann, and T. W. Kephart, Gravitational waves from a black hole orbiting in a wormhole geometry, *Phys. Rev. D* **104**, 044030 (2021).
 - [40] M. N. Malik, J. B. Dent, W. E. Gabella, and T. W. Kephart, Gravitational Waves from a Black Hole Falling Radially into a Thin-Shell Traversable Wormhole, arXiv: 2605.01216 [10.48550/arxiv.2605.01216](https://arxiv.org/abs/2605.01216) (2026).
 - [41] P. F. Byrd and M. D. Friedman, Handbook of Elliptic Integrals for Engineers and Scientists (Springer Berlin, Heidelberg, 1971).
 - [42] Y. Mino, Perturbative approach to an orbital evolution around a supermassive black hole,

- Phys. Rev. D* **67**, 084027 (2003).
- [43] V. Cardoso, A. S. Miranda, E. Berti, H. Witek, and V. T. Zanchin, Geodesic stability, Lyapunov exponents, and quasinormal modes, *Phys. Rev. D* **79**, 064016 (2009).
- [44] W.-C. Syu, D.-S. Lee, and C.-Y. Lin, Regular and chaotic behavior of collective atomic motion in two-component Bose-Einstein condensates, *Phys. Rev. A* **101**, 063622 (2020).